Novel Role for Vinculin in Ventricular Myocyte Mechanics and Dysfunction

Jared R. Tangney,[†△] Joyce S. Chuang,[†△] Matthew S. Janssen,[†] Adarsh Krishnamurthy,[†] Peter Liao,[‡§] Masahiko Hoshijima,[‡‡‡] Xin Wu,[¶] Gerald A. Meininger,[||] Mariappan Muthuchamy,[¶] Alice Zemljic-Harpf,[‡§] Robert S. Ross,[‡§‡‡] Lawrence R. Frank,[††] Andrew D. McCulloch,[†‡‡‡] and Jeffrey H. Omens[†‡‡‡*]

[†]Department of Bioengineering and [‡]Department of Medicine, University of California-San Diego, La Jolla, California; [§]Veterans Administration Healthcare San Diego, San Diego, California; and [¶]Department of Systems Biology and Translational Medicine, Texas A&M Health Science Center, College of Medicine, College Station, Texas; [||]Dalton Cardiovascular Research Center and Department of Medical Pharmacology and Physiology, University of Missouri, Columbia, Missouri; [††]Department of Radiology and [‡‡]Cardiac Biomedical Science and Engineering Center, University of California-San Diego, La Jolla, California

ABSTRACT Vinculin (Vcl) plays a key structural role in ventricular myocytes that, when disrupted, can lead to contractile dysfunction and dilated cardiomyopathy. To investigate the role of Vcl in myocyte and myocardial function, cardiomyocyte-specific Vcl knockout mice (cVclKO) and littermate control wild-type mice were studied with transmission electron microscopy (TEM) and in vivo magnetic resonance imaging (MRI) tagging before the onset of global ventricular dysfunction. MRI revealed significantly decreased systolic strains transverse to the myofiber axis in vivo, but no changes along the muscle fibers or in fiber tension in papillary muscles from heterozygous global Vcl null mice. Myofilament lattice spacing from TEM was significantly greater in cVclKO versus wild-type hearts fixed in the unloaded state. AFM in Vcl heterozygous null mouse myocytes showed a significant decrease in membrane cortical stiffness. A multiscale computational model of ventricular mechanics incorporating cross-bridge geometry and lattice mechanics showed that increased transverse systolic stiffness due to increased lattice spacing may explain the systolic wall strains associated with Vcl deficiency, before the onset of ventricular dysfunction. Loss of cardiac myocyte Vcl may decrease systolic transverse strains in vivo by decreasing membrane cortical tension, which decreases transverse compression of the lattice thereby increasing interfilament spacing and stress transverse to the myofibers.

INTRODUCTION

Vinculin (Vcl) is a 117-kDa membrane-associated protein expressed in all cell types. It localizes at both cell-matrix and cell-cell adhesion sites including costameres and intercalated disks in cardiomyocytes (1–3). Vcl is a key structural component in the formation of costamere protein complexes that link the actin cytoskeleton to integrins on the cell surface of muscle cells (4–7). Vcl mutations have been linked to both hypertrophic and dilated cardiomyopathies in humans (8). Previous studies have shown that suppression of Vcl expression by antisense oligonucleotide treatment of fetal cardiomyocytes causes a disturbance in normal myofibrillar arrangement (9). Additionally, investigation of heterozygous global Vcl knockout mice (VclKO) showed normal basal cardiac function, abnormal intercalated disks, and a predisposition toward stress-induced cardiomyopathy provoked by aortic constriction (5). The mouse model utilized in this study has cardiomyocyte-specific reduction of Vcl (cVclKO) and displays abnormal intercalated disks (4). Half of the cVclKO mice die suddenly, before the age of three months, and the remainder develop dilated cardiomyopathy (DCM) by 16 weeks of age (4). The normal expression of Vcl may allow cells to resist stresses that result from mechanical forces on the cell exterior (4), suggesting a structural role in force transmission between the exterior and interior of the myocyte. It has also been suggested that Vcl plays a significant role in mechanotransduction (5). Therefore Vcl deficiency may contribute to the development of ventricular remodeling leading to DCM, as was shown in the cVclKO mice. In addition to transducing mechanical signals, Vcl could directly affect mechanical function of the myocardium in a direction-dependent manner owing to its localization at the costamere, where it may contribute to the balance of myocyte forces between cortical membrane tension and transverse myocyte stresses.

To better understand the role of Vcl in regional cardiac function, the three-dimensional geometric structure of the heart and fiber architecture must be taken into account. Muscle fibers have a distinct helical pattern in the wall of the left ventricle (10). In addition to fiber orientation, endomysial collagen struts link costameres of adjacent cells in the transverse direction (11) forming a laminar sheet structure (10), and may be key to the transmission of forces transverse to the cells. Therefore, weakening of cell-extracellular matrix interactions or redistribution of intracellular forces, as could occur when cells have deficiencies in Vcl, may directly affect mechanics transverse to the myocyte fiber axis.

The goal of this study was to investigate the structural role of Vcl in cardiac myocytes, and to determine the implications for regional mechanics before the onset of global ventricular pump dysfunction in Vcl knockout mice. We hypothesized that altered cytoskeletal structure or force

Submitted August 22, 2012, and accepted for publication February 7, 2013.

△Jared R. Tangney and Joyce C. Chuang contributed equally to this article.

*Correspondence: jomens@ucsd.edu

Editor: Peter Hunter.

0006-3495/13/04/1623/11 $2.00

http://dx.doi.org/10.1016/j.bpj.2013.02.021

transmission may affect tissue mechanics relative to the muscle fiber structure. Studying these animals before they develop heart failure allows more direct examination of the role of the protein defect, before secondary effects of heart failure complicate the physiological response. Measurements of regional strains and isolated muscle mechanical properties may also reveal early contractile defects that are compensated at the scale of whole ventricular pump function. Three-dimensional cardiac strains were measured in vivo with magnetic resonance imaging (MRI) tagging in control and cVclKO mice at an age of 6–7 weeks before the onset of DCM in cVclKO. There were significant decreases in end-systolic transverse (radial and cross-fiber) strain components with no changes in fiber strains, and no changes in global systolic function. The structural basis of this dysfunction was examined with ultrastructural quantification of sarcomere lattice spacing and AFM measurements of myocyte membrane mechanics. A multiscale computational model showed that the measured increases in lattice spacing that occurred with Vcl deletion could explain the observed alterations in three-dimensional ventricular wall mechanics by increasing the angle between strongly bound crossbridges and the myofilaments thereby stiffening the lattice transversely during systole. The results suggest that the primary effect of Vcl deficiency on myocyte mechanics is not on axial shortening or force development. Rather, by decreasing membrane cortical tension, loss of Vcl increases lattice spacing and transverse force development by the sarcomeres, which in turn compromises regional myocardial strains in the cross-fiber and radial directions. These findings suggest a novel sarcomere-level structural mechanism for myocardial mechanical dysfunction that may also be important in the early pathogenesis of heart failure associated with cytoskeletal defects.

MATERIALS AND METHODS

Mice

The cVclKO mice with cardiomyocyte-specific excision of the Vcl gene have been described previously (4). Cre-negative littermates (WT) with no Vcl excision were used as the controls. The mice used in this study were 6–7 weeks of age from strains that had been maintained in a mixed SV129/Black Swiss background and interbred for at least 10 generations. All protocols were performed according to the National Institute of Health's *Guide for the Care and Use of Laboratory Animals* and was approved by the University of California-San Diego's Animal Subjects Committee.

MRI and global function

MRI protocols for cine and tagging sequences were based on the methods in Chuang et al. (12) (see the Supporting Material for details). A sample tagged image at end-systole is shown in Fig. 1 *A*. In the cine images, the myocardium was segmented with a semiautomatic level set algorithm (13) to extract the endocardial and epicardial boundaries. A three-dimensional geometric model of the end-diastolic left ventricle (LV) was created (Fig. 1 *B*) by fitting high-order prolate spheroidal finite element meshes to the endocardial and epicardial points (12). Cavity and wall volumes were measured from the three-dimensional mesh, and wall mass was calculated by multiplying wall volume with myocardial density (1.05 g/mL) (11).

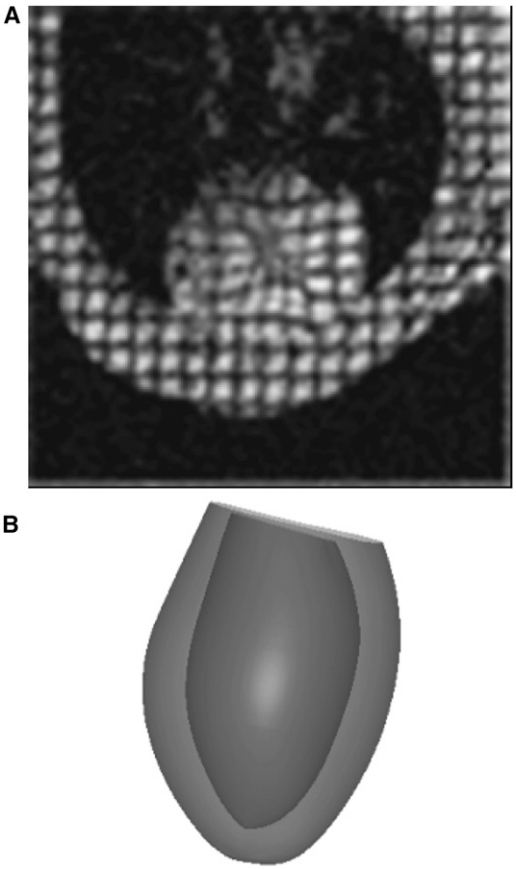

FIGURE 1 (*A*) MRI tagging of the mouse heart at end-systole showing deformed tag lines in a short-axis view predominantly of the LV wall (*circular cross-section*) and the nontagged (*shaded*) area of the LV chamber. (*B*) Three-dimensional geometric model of the mouse LV used for global parameter estimation.

Fiber strain analysis

Harmonic phase (HARP) analysis was used to automatically track myocardial material points in the SPAMM images (14). To calculate three-dimensional Lagrangian strains, a deformable model was created using material point displacements from the HARP analysis. The end-diastolic LV model was deformed to fit material point coordinates at end-systole. End-systolic strains with respect to the cardiac coordinates (circumferential, longitudinal, and radial) were calculated at the equator (midventricle) of the LV free wall, at five transmural locations (epicardial, subepicardial, midwall, subendocardial, and endocardial). Strains were then rotated about the radial axis through the measured fiber angle (see measurements below) to give regional strain in cardiac fiber coordinates (fiber, cross-fiber, and radial axes; as seen in Fig. S5 in the Supporting Material). Details of the implementation of the deformable model can be found in Chuang et al. (12).

Histology

After MRI, hearts were arrested and fixed for measurement of fiber and laminar sheet angles (see the Supporting Material for details).

Isolated muscle mechanics

Right ventricular papillary muscles were isolated from adult WT and heterozygous global Vcl null hearts, and mounted in a cardiac tissue culture chamber as previously described in Raskin et al. (15). After preconditioning, the muscles were stimulated at 1 Hz, and stretched from slack length to a passive muscle length with maximum developed systolic force. Peak isometric twitch force was recorded at several passive lengths along with muscle cross-sectional area to determine peak developed fiber stress as a function of passive length.

AFM for cell membrane stiffness and adhesion force

AFM was performed in cardiomyocytes isolated from adult WT and heterozygous global Vcl null hearts. In a third group vinculin gene transfer was performed in heterozygous null myocytes. The force contact mode of operation was used to measure adhesion force and cortical membrane stiffness (elastic modulus) from the retraction and approach curves, respectively (16–18) (see the Supporting Material for details).

Myofilament image analysis

Samples were prepared for transmission electron microscopy (TEM) using standard techniques (see the Supporting Material for details). Groups of cVclKO and WT hearts were fixed either in diastole (arrested) or in systole (barium contracture). Sarcomere length (SL) images and myofibril interfilament lattice spacing images were recorded with TEM, and a fast Fourier transform technique was used to measure lattice spacing from diffraction patterns (see the Supporting Material for details).

Myofilament lattice mechanics model

A micromechanical model of myofilament mechanics was used to derive transverse systolic sarcomere stiffness as a function of cross-bridge stiffness based on cross-bridge geometry and actomyosin lattice spacing (Fig. 2). Similar to the analysis by Schoenberg (19), transverse and axial cross-bridge forces were resolved using a simplified two-dimensional model where the S2 segment was modeled as a spring with a freely jointed hinge at the origination site on the thick filament backbone with an axial tilt angle at the attachment site (α, Fig. 2, *A* and *B*) of 45° (20,21). Because the S2 origin site was modeled as a freely rotating pivot point, the angle between the thick filament and the S2 region of myosin (θ in Fig. 2, *E* and *F*) is constrained by the other angles and varies as a function of actin-myosin lattice spacing (Δ). These assumptions are sufficient to allow the cross-bridge force F_{S2} to be resolved into longitudinal (fiber) and cross-fiber (transverse) force components, F_f and F_t, respectively. An increase in lattice spacing increases the cross-bridge tension by increasing cross-bridge strain and increases the ratio of F_t to F_f by increasing θ (Fig. 2, *A* and *B*). The changes to F_t and F_f resulting from an incremental increase in Δ gives the transverse and fiber cross-bridge stiffnesses whose ratio is

$$\frac{K_t}{K_f} = \frac{l_{S2} - \hat{l}_{S2}\cos^2\theta}{l_{S2} - \hat{l}_{S2}\sin^2\theta}, \quad (1)$$

where l_{S2} and $\hat{l}_{S2}$ are the instantaneous and resting lengths of the S2 segment of myosin, respectively.

To compute macroscopic three-dimensional transverse/fiber stiffness ratios, we next consider the myofilament lattice geometry in planes transverse and parallel to the myofilaments (Fig. 2, *C* and *C*) when all cross-bridges are attached in the strongly bound state. By deriving the strain energy associated with equibiaxial transverse strain of the lattice and uniaxial fiber strain of the sarcomeres (see the Supporting Material for details), we obtain the following expression for the ratio of the transverse lattice stress (σ_{tt}) to the fiber lattice stress (σ_{ff}),

$$\frac{\sigma_{tt}}{\sigma_{ff}} = \frac{1}{2}\left(\frac{\Delta}{\delta}\right)\frac{K_t}{K_f}, \quad (2)$$

where δ is the distance along the thick filament between consecutive cross-bridge pairs in the same plane (Fig. 2 *E*) and also represents the length of a hexagonal unit element, with six crossbridges (three pairs) and a radius equal to the actin-myosin lattice spacing (Δ) (Fig. 2, *C* and *D*).

To use these expressions in a continuum constitutive model of systolic myocardial stress, the SL to be used is calculated from the macroscopic fiber strain using the unloaded reference sarcomere length (S_0) that was measured for each genotype from the electron micrographs of unloaded cardioplegia-arrested hearts. The time-varying myofilament lattice spacing was computed from the sarcomere length (S) using the assumption that sarcomere volume (V_S) remains constant during the cardiac cycle, i.e., $S \times \Delta^2 = V_S$. The volume constant V_S for each genotype was based directly on TEM measurements in the diastolic and systolic arrested preparations, which also supported the assumption that the lattice deformed isotropically during contraction (i.e., even though the ventricle thickened radially and

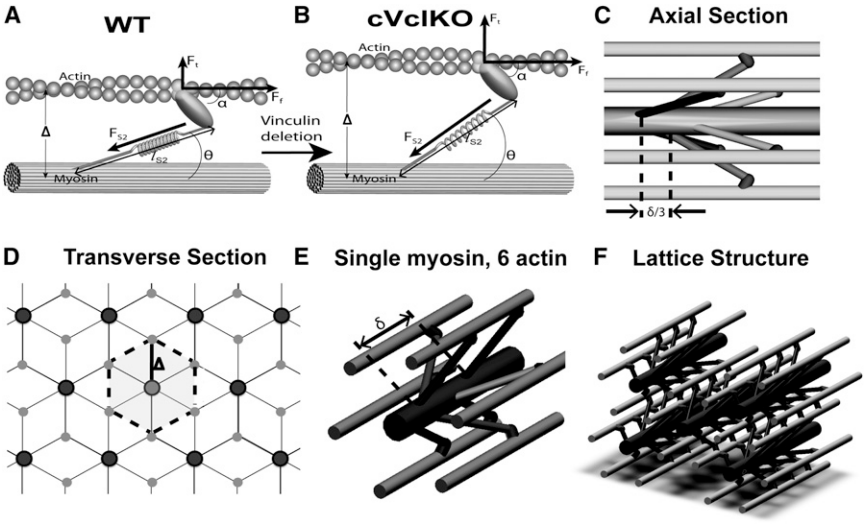

FIGURE 2 Micromechanical model for sarcomere lattice spacing and cross-bridge architecture. (*A*) Individual cross-bridge model consisting of a myosin stalk based on the geometry by Schoenberg (19). (*B*) As the lattice spacing (Δ) increases with Vcl deletion (transition from panels *A* to *B*), binding angles (θ) change and F_{S2} increases, and attachment angle α remains constant. The result is an increase in the transverse force, but little change in the fiber force (F_t = transverse force, F_f = fiber force, F_{S2} = force along S2 segment). (*C* and *D*) The unit cell of the lattice structure in the axial (*C*) and transverse (*D*) directions is marked (*dotted outline*, δ = 3 pairs of myosin heads spacing). (*E*) A single myosin filament is surrounded by six actin filaments. (*F*) Overall lattice structure. Details of this myofilament lattice model can be found in the Supporting Material.

shortened transverse to the fibers in the plane of the wall, the interfilament distances remained independent of orientation in the plane transverse to the filaments). V_S, derived from the electron micrographic measurements, was scaled up by 20% in both genotypes to account for the effects of lattice shrinkage due to dehydration and fixation previously reported by several groups using similar techniques, which only affects lattice spacing and not the SL (22–24).

In summary, by considering the mechanical equilibrium of the cross-bridge and myofilament lattice in three dimensions, we derived a micromechanical model for myocyte systolic stiffnesses in the fiber and transverse directions as a function of sarcomere length and lattice spacing. A kinematic model in turn enables the SL and lattice spacing to be determined from macroscopic fiber strains. The only parameters in this analysis that were varied between genotypes were the SL and V_s (calculated from SL and Δ) as measured directly from the electron micrographs.

Ventricular mechanics model

This microstructural model was included in a finite element model of ventricular mechanics to test whether measured alterations in sarcomere geometry were sufficient to explain observed mechanics in vivo in young WT and VclKO mice. The left ventricle was approximated by a truncated prolate spheroidal geometry and fiber orientations were included based on the histological measurements. Systolic active muscle stress was computed as a function of time and regional fiber strain using a previously published model (25) with parameters that were the same for both genotypes as given in the Supporting Material. Using measured SL and lattice spacing the dynamic transverse stiffness was computed from the model fiber stress using the ratio obtained above from the micromechanical model. The ventricular model was coupled to a Windkessel model of aortic impedance and used to compute regional wall stresses and strains and ejection fractions (see the Supporting Material for details).

Statistics

All measurements are presented as mean ± SD. End-systolic strains, sarcomere geometry measurements between cVclKO and WT mice, and fiber angles were compared by two-way repeated measures analysis of variance (ANOVA). P-values < 0.05 were considered significant. To identify the effects of genotype on Δ independent of differences in SL, the relationship was analyzed using analysis of covariance (ANCOVA) in which the regressor was $1/\sqrt{SL}$ based on the assumption of sarcomere volume conservation. To test the statistical significance of the results predicted by the model, z-scores were assigned to all the model strain results based on the experimental means and standard deviations, and used to determine if model results fall within the experimental variance.

RESULTS

Global geometry and function

From the geometric models based on the cine MRI images of the myocardium, end-diastolic volume (EDV), end-systolic volume (ESV), ejection fraction (EF), and left-ventricular mass index (LVMI) were measured ($n = 5$ for both WT and knockout (KO)). EDV (48 ± 12 vs. 50 ± 11 μL) and ESV (20 ± 8 vs. 25 ± 6 μL) were slightly larger in cVclKO, but not significantly different. There were also no significant differences in EF (50 ± 4 vs. 58 ± 9%) and LVMI (4.2 ± 0.9 vs. 4.1 ± 0.7 mg/g) between cVclKO and WT mice, respectively. Mean lung/body weight ratios (0.60 ± 0.11%, WT and 0.64 ± 0.09%, KO) and liver/body weight ratios (3.73 ± 0.43%, WT and 4.05 ± 0.67%, KO) were not different between the groups. Peak systolic fiber stress was not different at any passive muscle length as determined from isolated papillary muscle studies (see the Supporting Material for data).

Fiber and sheet angles

Mean fiber angles at the equator of the LV free wall measured from histology displayed a linear transmural distribution between ~−65° at the epicardium and +65° at the endocardium with no differences between cVclKO and WT hearts ($n = 5$ in each group). Sheet angles were on average negative throughout the wall, varying from −42° to −65° at the midventricle, similar to previously reported values (26). There were no significant differences in sheet angles between cVclKO and WT hearts. Both fiber and sheet angle measurement results can be seen in Fig. S1.

Regional strains

Regional midventricular strain tensors computed from the HARP analysis at three transmural locations and resolved with respect to local fiber coordinates (f = fiber, c = cross-fiber, r = radial), using the measured fiber angles, are shown in Fig. 3 at end-systole (referred to as an undeformed reference state at end-diastole). In WT mice, systolic fiber strain (E_{ff}) was negative (shortening) and uniform across the wall. Cross-fiber strain (E_{cc}) was also negative as expected and radial strain (E_{rr}) was positive, consistent with systolic wall thickening, and both of these components were largest at the endocardium and smallest at the epicardium, as seen previously in the mouse (12) and other species (27). In cVclKO hearts, two-way ANOVA analysis for the strain components (Table 1) showed that E_{ff} was not different from WT; however, the transverse components of strain (E_{cc} and E_{rr}) showed significant differences of interaction ($n = 5$, $p = 0.010$, and $p = 0.001$, respectively), implying a difference in the way the strains vary transmurally. E_{rr} in the cVclKO hearts decreased in magnitude with wall depth, opposite of the gradient observed in the WT hearts. There was also a significant difference ($p < 0.001$, $n = 5$) between genotypes regardless of transmural location for E_{rr}. All of the shear strains were relatively small in magnitude, but a genotype difference was observed for both E_{fc} and E_{cr} ($n = 5$, $p = 0.002$ and $p = 0.015$, respectively). Overall, Vcl deficiency significantly reduced myocardial systolic strains transverse to the myocytes but had no effect on systolic fiber shortening.

Membrane stiffness and adhesion force with AFM

Cortical membrane stiffnesses were computed from force curve data (see Fig. S3, with more details in the Supporting

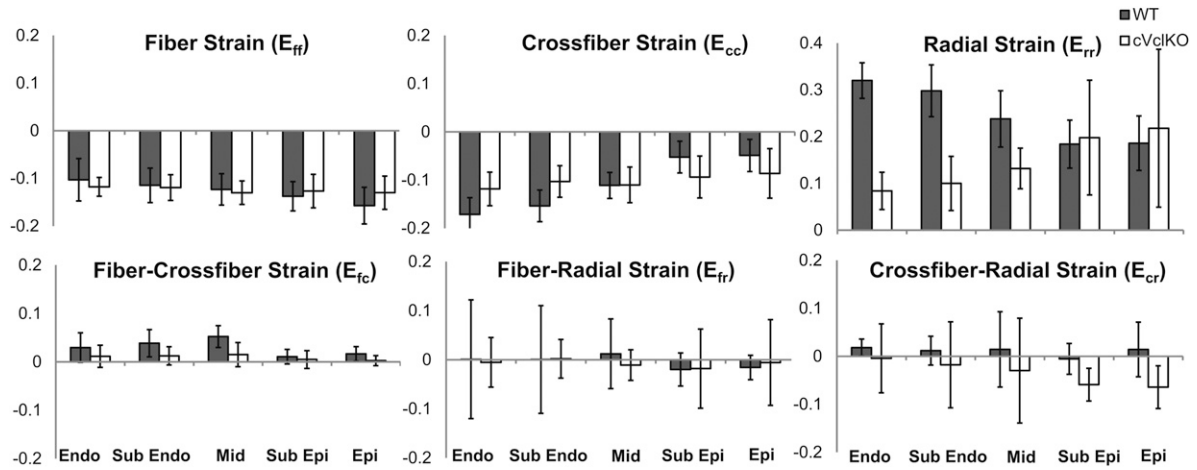

FIGURE 3 Regional end-systolic fiber strains found from MRI and three-dimensional model analysis at five transmural locations ($n = 5$). Six strain components are referenced to the local fiber coordinate system (f = fiber, c = cross-fiber, and r = radial axes). Values and gradients for WT are as expected, and statistical comparison between WT (*solid*) and cVclKO (*open*) shows decreases in strain magnitude predominately for the radial strains (E_{rr}). (*Endo*, endocardium; *epi*, epicardium; *mid*, midwall.)

Material). Stiffness in cardiomyocytes from Vcl heterozygous null mice (14.8 ± 0.6 kPa) decreased significantly by 55% compared with WT myocytes (32.5 ± 1.2 kPa, $n = 10$). Rescue of vinculin restored cell stiffness to control levels (34.5 ± 0.9 kPa, $n = 10$). There were no significant changes in the initial peak adhesion force among Vcl null (39.1 ± 0.2 pN, $n = 10$), vinculin rescued (39.9 ± 0.9 pN, $n = 10$), and WT myocytes (38.6 ± 1.6 pN, Fig. 4 *B*). The probability of adhesion to extracellular matrix protein fibronectin decreased significantly by 40% in Vcl heterozygous null myocytes compared with WT, and this difference was no longer significant in myocytes in which vinculin expression was rescued.

Sarcomere geometry

Myofilament lattice dimensions measured from optical diffraction patterns computed from transmission electron micrographs (Fig. 5 *A*) are shown in Table 2 ($n = 3$ for both WT and KO). Actin-myosin lattice spacing obtained from the second-order diffraction distance and myosin-myosin lattice spacing (M-M Δ) from the first-order diffraction pattern were both larger for cVclKO mice than WT animals. The mean ratio of (M-M Δ)/Δ (1.70) was within 1.9% of $\sqrt{3}$, the ratio as derived for a hexagonal lattice. Sarcomere lengths were slightly lower ($p = 0.051$) in the KO mice, so to compare lattice dimensions independent of SL we plotted Δ vs. $1/\sqrt{SL}$ (Fig. 5 *B*). The slope of this relation is the sarcomere volume constant V_S ($p = 0.59$ between WT and cVclKO). There was no significant effect of genotype or contractile state on sarcomere volume. By ANCOVA

TABLE 1 Two-way ANOVA *p*-value results show the difference between WT and cVclKO strains based on the five locations through the wall and genotype

Strain component	Genotype	Wall location	Interaction
E_{ff}	0.799	0.210	0.638
E_{cc}	0.618	<0.001[a]	0.010[a]
E_{rr}	<0.001[a]	0.976	0.001[a]
E_{fc}	0.002[a]	0.053	0.548
E_{fr}	0.879	0.965	0.990
E_{cr}	0.015[a]	0.629	0.871

[a]Statistically significant values ($p < 0.05$).

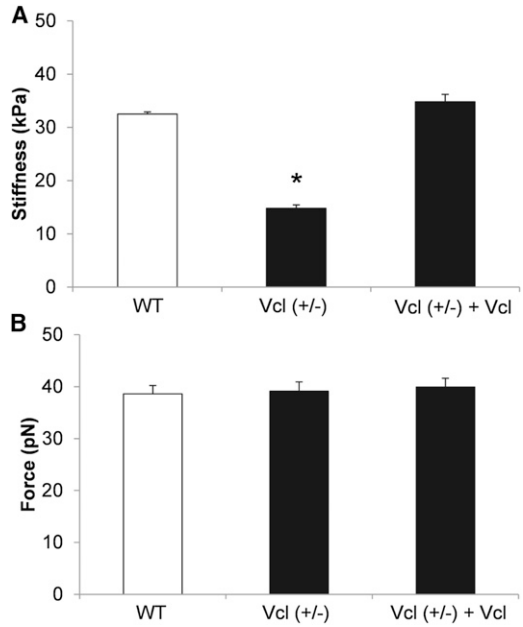

FIGURE 4 AFM measurements in cardiomyocytes from wild-type (WT), heterozygous null (Vcl+/−), and vinculin rescued (Vcl+/− + Vcl) groups. (*A*) Cell cortical stiffness was significantly decreased in Vcl+/− mouse cardiomyocytes. Rescue of vinculin expression in Vcl +/− cardiomyocytes restored stiffness to WT levels. (*B*) Adhesion force was not changed in the three groups. *$p < 0.05$ vs. WT. $n = 10$ for each group.

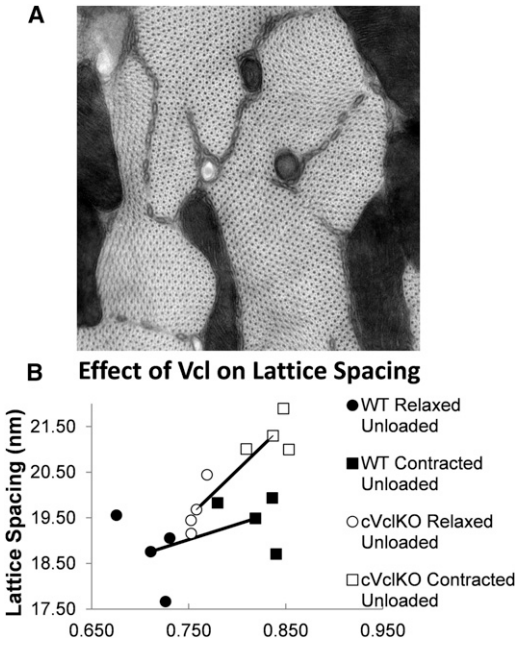

FIGURE 5 Lattice spacing image analysis. (*A*) Representative TEM image montage at ×47,000 magnification showing myofilament cross-sections of a relaxed unloaded cVclKO heart. The pixel size is 0.19 nm, and the image size is 2.3 μm × 2.3 μm. (*B*) Effect of Vcl deletion on actin-myosin filament spacing in mouse hearts arrested at end-diastolic (smaller $1/\sqrt{SL}$) and barium-contracted states (larger $1/\sqrt{SL}$). Assuming constant volume, Δ varies with $1/\sqrt{SL}$. (*Line*) Connection of average points.

there was a significant effect of genotype and a significant effect of contractile state on both myosin-myosin lattice spacing and Δ. Refer to Table 2 for all *p*-values.

Ventricular strains from model analysis

Table S1 in the Supporting Material summarizes all of the myofilament lattice mechanics as well as the finite element model parameters; the only parameters that were different between the models of the WT and cVclKO mice were those derived from the electron micrographs: unloaded reference SL (1.88 μm WT and 1.74 μm cVclKO), unloaded systolic SL (1.50 μm WT and 1.43 μm cVclKO), and volume constant V_S from which lattice spacing was computed (1620 nm^2/μm WT and 2030 nm^2/μm cVclKO). End-systolic strain components in fiber/cross-fiber coordinates referred to as end-diastole are shown in Fig. 6 for WT and cVclKO models and compared with experimental results from the MRI tagging experiments. Fiber strains computed with the models showed a slightly larger difference between WT and cVclKO than what was observed experimentally. The radial strain decreased substantially with the increased lattice spacing, but the reversal in the transmural gradient that was observed experimentally was not quite captured by the model. The cross-fiber strain decreased at the endocardium and midwall, but increased slightly at the epicardium with an increase in lattice spacing due to loss of Vcl, similar to the trend that was observed experimentally. In the simulation, end-systolic fiber stresses in the cVclKO model were 11% higher on average through the wall compared to WT, where the largest increase was seen at the epicardium (22%) and the smallest decrease was in the midwall (2%).

Z-scores showed that model results were within two standard deviations of the mean experimental values for all six strain components at all transmural locations ($z < 2$) except for 1 of the 60 component/location combinations. In addition to the systolic strains, the model predicted an EF of 44% for WT and 35% for cVclKO. Statistical analysis of model-predicted values using the variance of the experimental EF showed no difference ($p = 0.06$), similar to the experimental finding ($p = 0.08$).

DISCUSSION

In this study, we examined the effect of Vcl deletion and Vcl deficiency on myocyte and ventricular mechanics before the onset of global ventricular dysfunction in cVclKO mice. At this time we expected that Vcl deficiency is the main cause of the structural defects at the sarcomere level. The mechanistic multiscale model analysis and experimental results suggest that the observed early alterations in myocardial systolic wall strains transverse but not parallel to the myofibers can be explained by the observed increase in systolic and diastolic myofilament lattice spacing. As the angle

TABLE 2 Sarcomere length (SL), myosin-myosin lattice spacing (M-M Δ), and actin-myosin lattice spacing (Δ) raw measurements for cVclKO ($n = 3$) and WT ($n = 3$) hearts arrested at end-diastole, and hearts contracted with barium (Ba) against zero load ($n = 3$ each for WT and cVclKO)

		M-M Δ(nm)	Δ (nm)	SL (μm)
Relaxed unloaded hearts	VclKO (Avg ± SD)	33.47 ± 1.35	19.67 ± 0.68	1.74 ± 0.04
	WT (Avg ± SD)	30.83 ± 0.68	18.76 ± 0.98	1.99 ± 0.18
Ba-contracted unloaded hearts	VclKO (Avg ± SD)	37.61 ± 2.39	21.30 ± 0.52	1.43 ± 0.08
	WT (Avg ± SD)	32.90 ± 1.57	19.49 ± 0.68	1.50 ± 0.13
		M-M Δ	Δ	
	Two-way ANCOVA (*p*-value)	0.0333	0.0446	

The ANCOVA results show a significant genotype difference, for both M-M Δ and Δ.

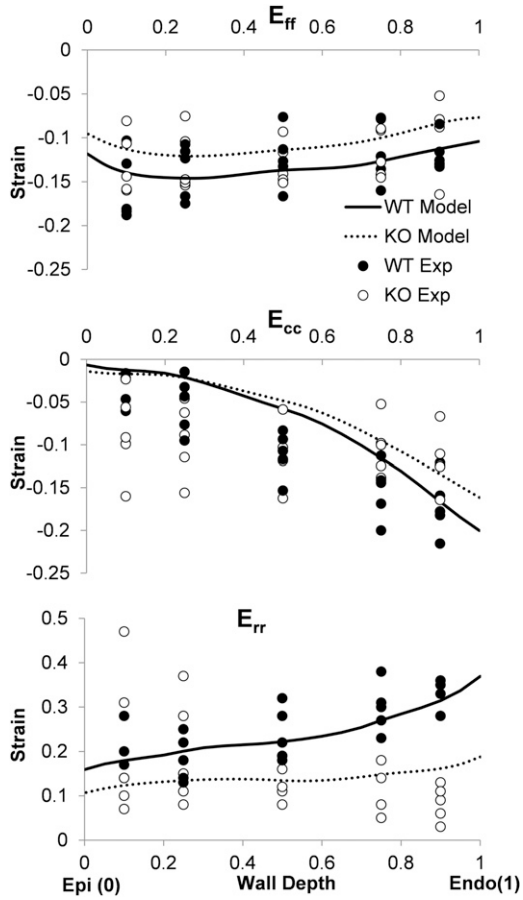

FIGURE 6 Model versus experiment comparison of fiber (E_{ff}), cross-fiber (E_{cc}), and radial (E_{rr}) systolic strains. Gradients and magnitudes are mostly similar, indicating general agreement between model and experiment.

between the thick filament and the S2 region increases with increased lateral myofilament spacing, the radial component of the force in the crossbridge increases with little change in the axial component. The lattice model suggests that this results in a comparable increase in transverse systolic stiffness relative to fiber stiffness at the level of the myocyte. The ventricular model suggests that these anisotropic changes in systolic stiffness due to Vcl deletion result in little change in systolic fiber shortening but a substantial decrease in radial wall thickening during systole—which is now being opposed by the higher radial stiffness of the lattice in the cVclKO mice. Changes in shear strains were small in the model and hence, owing to incompressibility, similar fiber shortening and decreased radial thickening resulted in decreased cross-fiber shortening in the cVclKO mouse model.

Consistent with this hypothesis, papillary muscle tests showed no changes in isometric tension in global Vcl heterozygous null mice compared with controls. Atomic force microscopy in global Vcl heterozygous null myocytes showed a decrease in the probability of binding to fibronectin-coated probe tips but no change in the force of adhesion, suggesting a decreased expression, availability, or affinity of integrin receptors. However, membrane cortical stiffness calculated from the AFM force curves showed a significant decrease in Vcl heterozygous null myocytes that was reversed when vinculin expression was rescued in vitro. We suggest here that this finding may be due to a decrease in membrane cortical tension that is in equilibrium with transverse compression of the myofilament lattice that is presumably transmitted via the Z-disk. The location of Vcl in relation to the Z-disk, myofilaments, and the cell membrane as well as its possible role in membrane tension can be seen in Fig. 7. When vinculin is deleted, there is a decrease in the stiffness of the protein complex at the costamere which causes a decrease in the cortical tension, allowing for Z-disk expansion (increasing the lattice spacing). By decreasing membrane cortical tension, the lattice compression is relieved, resulting in expansion that increases actin-myosin lattice spacing. Hence, we conclude that an early mechanism of ventricular mechanical dysfunction before the onset of heart failure in vinculin-deficient mice is an increase in systolic transverse myofiber stress development due to increased myofilament lattice spacing mediated by a decrease in membrane cortical tension. In the cVclKO model, the change in material properties led to a 13% increase in the subendocardial systolic fiber stress. Because increased wall stress is a known risk factor for hypertrophy and cardiac dilation, these structural changes could contribute to the subsequent development of heart failure in cVclKO mice.

Global cardiac function in 6–7-week-old WT mice, as shown by EDV and EF derived from MRI, were near the ranges reported in literature (28–30). Slight differences may be attributed to background strain, age, and anesthesia levels. On average, cVclKO hearts were slightly larger than WT hearts and EF was minimally lower, but there were no significant differences detected in any of the global parameters. Therefore, loss of Vcl did not significantly affect global systolic function or geometry in the animals studied here.

The measured three-dimensional end-systolic strains in the WT free wall agree well with previously published mouse data in terms of magnitude and sign (31,32). Our WT strains showed that E_{rr} is positive, indicating systolic wall thickening, and in general larger at the endocardium than the epicardium. In-plane strains were negative as expected, and torsional strain was also as seen before (30). Fiber architecture in the cVclKO hearts was not different from that found in control hearts, and was consistent with previously published mouse studies (26). Transforming strains into fiber coordinates provides insight into fiber and transverse-myocyte mechanics. The sign and magnitude of systolic fiber strain components in WT mice were similar to values measured in large animals such as the dog (27,33). In cVclKO mouse hearts, end-systolic E_{ff} strain was not

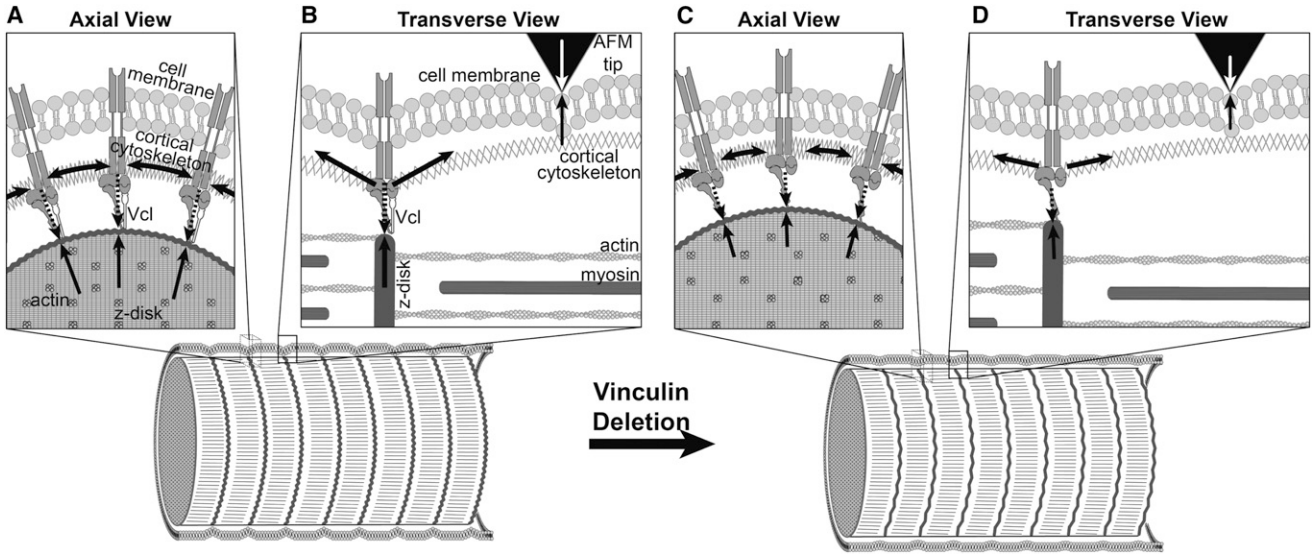

FIGURE 7 A hypothesized model of a possible role for vinculin in membrane cortical tension and compression of the Z-disk. In this model, vinculin maintains tension in the cortical cytoskeleton which compresses the Z-disk. When vinculin is deleted, the stiffness and force of the protein complex at the costamere (*long dashed downwardarrows in panels A and B*) is decreased (represented by *shorter dashed arrows* in panels *C* and *D*), which in turn leads to a decrease in the cortical tension (represented by *shorter horizontal solid arrows* in the cortical cytoskeleton in panels *C* and *D*), corresponding to lower AFM indentation force (*open arrows*). This decrease in cortical tension allows for the Z-disk to expand (owing to reduced compression of the Z-disk balanced by the reduced cortical tension). The expansion of the Z-disk leads to a larger lattice spacing.

significantly different from WT hearts, but E_{rr} and E_{cc} were decreased at several locations. This change in transverse function led to the hypothesis that sarcomere lattice spacing and myocyte force generation are altered by Vcl deficiency, and hence the histological and modeling studies.

Loss of normal Vcl expression led to increased myofilament lattice spacing that may be mediated by altered equilibrium of stresses in the cytoskeleton. On average, the myofilament lattice spacing in unloaded cVclKO hearts was larger than in the WT hearts at rest and in contracture, suggesting the presence of a cytoskeletal compressive prestress acting transverse to the filaments (tangentially to the Z-disk) that is partially released when Vcl is disrupted. Consistent with this hypothesis, membrane cortical stiffness measured by AFM was ~55% lower in global heterozygous Vcl null cardiomyocytes than controls, and this difference was lost when vinculin expression was restored in these cells. Wang et al. (34) suggested that membrane stiffness is primarily a result of cortical pretension in adherent contractile cells. This idea is consistent with the tensegrity hypothesis of cell mechanics (35) the details of which are debated, but consistent with a growing number of cell mechanical studies. Thus we propose here that a decrease in membrane stiffness and expansion of the myofilament lattice can be mediated by a decrease in membrane pretension transmitted via the Z-disk.

Previously, x-ray diffraction studies in rat heart muscle (36) reported a 34-nm distance between the planes of the thick filaments (d_{10} as described in Millman (24)) at a SL of 2.2 μm, which corresponds to a center-to-center distance between myosin filaments of 39 nm. Lattice spacing measurements from WT mice in this study were consistent (within 6%) with these values after accounting for expected lattice shrinkage due to TEM sample preparation methods (22–24). Although the WT TEM measurements were consistent with x-ray diffraction measurements, it should be noted that it is uncertain how lattice shrinkage due to TEM sample preparation might change with genotype or sarcomere length, which is a drawback to using TEM for this study. The lattice spacing in each mouse was also normalized by the inverse square-root of sarcomere length to exclude differences in lattice spacing due solely to differences in SL between preparations. Viewed this way, sarcomere volume was higher in cVclKO mouse cardiomyocytes irrespective of loading.

The micromechanical model used here assumed that the increased lattice spacing in the cVclKO hearts increases the cross-bridge angle, which would increase the transverse sarcomere stiffness and generated transverse force assuming no change in the location of the actin binding site. Because the location of the actin binding site was assumed to be the same between the two genotypes, the increased cross-bridge angle caused an increase in strain in the S2 segment of the myosin head. Owing to the fact that the S2 segment was modeled as a spring, the increased strain resulted in an increased force in this segment (as illustrated in Fig. 2). As a result, the cross-bridge active stress increased in the transverse direction but remained approximately constant along the fiber direction. This gave rise to a transverse stress on the lower end of the range recently determined by more

complex models of the crossbridge (37). This analysis implies that a more sophisticated model could show an even more dramatic increase in the transverse component of force with an increase in lattice spacing, possibly increasing the difference in E_{cc} between WT and cVclKO hearts.

The analysis of cross-bridge mechanics was performed using angles and geometric lengths that were either previously referenced in literature or measured in this study. The only values that were changed between the WT and cVclKO simulations were differences that were directly measured experimentally. No free or adjustable parameters were used to model the effects of Vcl deficiency in the active contraction simulations. The two-dimensional myosin segment lengths were obtained via a projection of a three-dimensional model using parameters from literature, and are referenced in Table S1.

The altered sarcomere geometry of the cVclKO mice results in decreased radial strain as predicted in the stress analysis of the crossbridge. However, a limitation of the model is that it does not predict the minor change in transmural gradient of E_{rr} between WT and cVclKO as seen experimentally. Fiber strain in the model simulation changes more between WT and cVclKO than the experiments, but the magnitudes of strain match the experiments very closely. The larger difference in fiber strain in the model shows the limitations of the simple model that could possibly be improved in the future with a more complex model. The cross-fiber strain is decreased in the cVclKO model throughout the wall, which agrees very closely to experiments at the endocardium, but the agreement differs slightly at the midwall and epicardium. This disagreement is most likely due to the high levels of variability in the measured cross-fiber strains. Additionally, it was determined that the increase in transverse active stress decreases the amount of wall thickening at end-systole when Vcl function is altered, which is consistent with experimental observations. The magnitudes of the genotypic strain changes in the simulation were less than the measured values, suggesting that the measured changes in sarcomeric structure may not be the only mechanism responsible for the altered ventricular function associated with Vcl deletion.

There are several limitations in this study. In the active contraction simulation the fiber angles were only measured at the equator; these angles were then incorporated throughout the model. In addition, no transmural SL gradient was included in the model because no data have been collected to show that it exists in the mouse model being studied. However, if it was determined that this gradient did exist, it would affect the accuracy of the SL measurements as previously described, and its absence would alter the simulation results. Also, the simplifying assumptions of the model (i.e., ignoring the higher-order sheet structure; modeling the myocardium as a transversely isotropic material; no fiber dispersion, etc.) together with the simple axisymmetric geometry of the mesh result in a model that may not be capable of accurately depicting all of the mechanistic subtleties associated with Vcl deletion. It should also be noted that the AFM stiffness protocol could be measuring a decrease in lattice stiffness as opposed to cortical tension; however, our analysis of lattice stiffness suggests that there would be an increase in systolic lattice stiffness in the transverse direction.

The results of this study are an important step in understanding the mechanistic link between cellular structural alterations and contractile dysfunction associated with Vcl deletion and Vcl protein deficiency before the onset of DCM remodeling. MRI tagging studies defined a specific mechanical defect in ventricular wall function that precedes any decrease in fiber shortening or global chamber function. This defect in mechanical function can be explained by a specific and measurable direction-dependent ultrastructural change at the sarcomere level due to loss of costamere-associated Vcl. AFM measurements suggest a direct mechanical link between this alteration in sarcomere geometry and the loss of costameric Vcl. We describe and quantitatively tested what is to our knowledge, an entirely novel mechanism for contractile dysfunction that may also explain how other proteins in the costamere and dystrophin-glycoprotein complex might lead to contractile dysfunction and subsequent cardiomyopathy.

SUPPORTING MATERIAL

Materials, methods, twelve equations, five figures, one table, and references (38-52).are available at http://www.biophysj.org/biophysj/supplemental/S0006-3495(13)00238-5.

The authors thank Jennifer Stowe and Taylor Coe for their expert technical assistance with these studies.

National Institutes of Health grants No. R01 HL103566, No. PO1 HL46345, grant No. HL088390, No. R01 HL105242, No. R01 HL96544, No. R21 EB003888-01A1, No. KO2 HL-86650, No. R01 MH096100, Veterans Administration grant No. BX001704, the National Biomedical Computation Resource grant No. P41 GM103426-19,Texas A&M Health Science Center Research Development Grant No. 244441-20702, and Electron microscopy was carried out at the National Center for Microscopy and Imaging Research (RR004050) and assisted by Mason Mackey.

REFERENCES

1. Rüdiger, M., N. Korneeva, …, B. M. Jockusch. 1998. Differential actin organization by vinculin isoforms: implications for cell type-specific microfilament anchorage. *FEBS Lett.* 431:49–54.
2. Schlaepfer, D. D., and T. Hunter. 1996. Signal transduction from the extracellular matrix—a role for the focal adhesion protein-tyrosine kinase FAK. *Cell Struct. Funct.* 21:445–450.
3. Hildebrand, J. D., M. D. Schaller, and J. T. Parsons. 1993. Identification of sequences required for the efficient localization of the focal adhesion kinase, pp125FAK, to cellular focal adhesions. *J. Cell Biol.* 123:993–1005.
4. Zemljic-Harpf, A. E., J. C. Miller, …, R. S. Ross. 2007. Cardiac-myocyte-specific excision of the vinculin gene disrupts cellular junctions,

causing sudden death or dilated cardiomyopathy. *Mol. Cell. Biol.* 27:7522–7537.

5. Zemljic-Harpf, A. E., S. Ponrartana, …, R. S. Ross. 2004. Heterozygous inactivation of the vinculin gene predisposes to stress-induced cardiomyopathy. *Am. J. Pathol.* 165:1033–1044.
6. Palmer, S. M., M. P. Playford, …, S. L. Campbell. 2009. Lipid binding to the tail domain of vinculin: specificity and the role of the N and C termini. *J. Biol. Chem.* 284:7223–7231.
7. Goldmann, W. H., R. Galneder, …, R. M. Ezzell. 1998. Differences in elasticity of vinculin-deficient F9 cells measured by magnetometry and atomic force microscopy. *Exp. Cell Res.* 239:235–242.
8. Zemljic-Harpf, A., A. M. Manso, and R. S. Ross. 2009. Vinculin and talin: focus on the myocardium. *J. Investig. Med.* 57:849–855.
9. Shiraishi, I., D. G. Simpson, …, T. K. Borg. 1997. Vinculin is an essential component for normal myofibrillar arrangement in fetal mouse cardiac myocytes. *J. Mol. Cell. Cardiol.* 29:2041–2052.
10. LeGrice, I. J., B. H. Smaill, …, P. J. Hunter. 1995. Laminar structure of the heart: ventricular myocyte arrangement and connective tissue architecture in the dog. *Am. J. Physiol.* 269:H571–H582.
11. Samarel, A. M. 2005. Costameres, focal adhesions, and cardiomyocyte mechanotransduction. *Am. J. Physiol. Heart Circ. Physiol.* 289: H2291–H2301.
12. Chuang, J. S., A. Zemljic-Harpf, …, J. H. Omens. 2010. Determination of three-dimensional ventricular strain distributions in gene-targeted mice using tagged MRI. *Magn. Reson. Med.* 64:1281–1288.
13. Yushkevich, P. A., J. Piven, …, G. Gerig. 2006. User-guided 3D active contour segmentation of anatomical structures: significantly improved efficiency and reliability. *Neuroimage.* 31:1116–1128.
14. Osman, N. F., W. S. Kerwin, …, J. L. Prince. 1999. Cardiac motion tracking using CINE harmonic phase (HARP) magnetic resonance imaging. *Magn. Reson. Med.* 42:1048–1060.
15. Raskin, A. M., M. Hoshijima, …, J. H. Omens. 2009. Hypertrophic gene expression induced by chronic stretch of excised mouse heart muscle. *Mol. Cell. Biomech.* 6:145–159.
16. Wolska, B. M., and R. J. Solaro. 1996. Method for isolation of adult mouse cardiac myocytes for studies of contraction and microfluorimetry. *Am. J. Physiol.* 271:H1250–H1255.
17. Wu, X., Z. Sun, …, M. Muthuchamy. 2010. Cardiomyocyte contractile status is associated with differences in fibronectin and integrin interactions. *Am. J. Physiol. Heart Circ. Physiol.* 298:H2071–H2081.
18. Wu, X., S. Chakraborty, …, M. Muthuchamy. 2011. Fibronectin increases the force production of mouse papillary muscles via $\alpha5\beta1$ integrin. *J. Mol. Cell. Cardiol.* 50:203–213.
19. Schoenberg, M. 1980. Geometrical factors influencing muscle force development. I. The effect of filament spacing upon axial forces. *Biophys. J.* 30:51–67.
20. Julian, F. J., R. L. Moss, and M. R. Sollins. 1978. The mechanism for vertebrate striated muscle contraction. *Circ. Res.* 42:2–14.
21. Rayment, I., H. M. Holden, …, R. A. Milligan. 1993. Structure of the actin-myosin complex and its implications for muscle contraction. *Science.* 261:58–65.
22. Irving, T. C., and B. M. Millman. 1992. Z-line/I-band and A-band lattices of intact frog Sartorius muscle at altered interfilament spacing. *J. Muscle Res. Cell Motil.* 13:100–105.
23. Palmer, B. M., B. K. McConnell, …, D. W. Maughan. 2004. Reduced cross-bridge dependent stiffness of skinned myocardium from mice lacking cardiac myosin binding protein-C. *Mol. Cell. Biochem.* 263:73–80.
24. Millman, B. M. 1998. The filament lattice of striated muscle. *Physiol. Rev.* 78:359–391.
25. Guccione, J. M., and A. D. McCulloch. 1993. Mechanics of active contraction in cardiac muscle: part I—constitutive relations for fiber stress that describe deactivation. *J. Biomech. Eng.* 115:72–81.
26. Omens, J. H., T. P. Usyk, …, A. D. McCulloch. 2002. Muscle LIM protein deficiency leads to alterations in passive ventricular mechanics. *Am. J. Physiol. Heart Circ. Physiol.* 282:H680–H687.
27. Ashikaga, H., J. H. Omens, …, J. W. Covell. 2004. Transmural mechanics at left ventricular epicardial pacing site. *Am. J. Physiol. Heart Circ. Physiol.* 286:H2401–H2407.
28. Croisille, P., C. Rotaru, …, B. Hiba. 2007. Gender and strain variations in left ventricular cardiac function and mass determined with magnetic resonance imaging at 7 tesla in adult mice. *Invest. Radiol.* 42:1–7.
29. Stegger, L., E. Heijman, …, G. J. Strijkers. 2009. Quantification of left ventricular volumes and ejection fraction in mice using PET, compared with MRI. *J. Nucl. Med.* 50:132–138.
30. Zhong, J., W. Liu, and X. Yu. 2009. Transmural myocardial strain in mouse: quantification of high-resolution MR tagging using harmonic phase (HARP) analysis. *Magn. Reson. Med.* 61:1368–1373.
31. Zhong, J., W. Liu, and X. Yu. 2008. Characterization of three-dimensional myocardial deformation in the mouse heart: an MR tagging study. *J. Magn. Reson. Imaging.* 27:1263–1270.
32. Young, A. A., B. A. French, …, F. H. Epstein. 2006. Reperfused myocardial infarction in mice: 3D mapping of late gadolinium enhancement and strain. *J. Cardiovasc. Magn. Reson.* 8:685–692.
33. Costa, K. D., Y. Takayama, …, J. W. Covell. 1999. Laminar fiber architecture and three-dimensional systolic mechanics in canine ventricular myocardium. *Am. J. Physiol.* 276:H595–H607.
34. Wang, N., I. M. Tolić-Nørrelykke, …, D. Stamenović. 2002. Cell prestress. I. Stiffness and prestress are closely associated in adherent contractile cells. *Am. J. Physiol. Cell Physiol.* 282:C606–C616.
35. Ingber, D. E., S. R. Heidemann, …, R. E. Buxbaum. 2000. Opposing views on tensegrity as a structural framework for understanding cell mechanics. *J. Appl. Physiol.* 89:1663–1670.
36. Irving, T. C., J. Konhilas, …, P. P. de Tombe. 2000. Myofilament lattice spacing as a function of sarcomere length in isolated rat myocardium. *Am. J. Physiol. Heart Circ. Physiol.* 279:H2568–H2573.
37. Williams, C. D., M. Regnier, and T. L. Daniel. 2010. Axial and radial forces of cross-bridges depend on lattice spacing. *PLOS Comput. Biol.* 6:e1001018.
38. Axel, L., and L. Dougherty. 1989. MR imaging of motion with spatial modulation of magnetization. *Radiology.* 171:841–845.
39. Jynge, P., D. J. Hearse, …, M. V. Braimbridge. 1981. The St. Thomas' hospital cardioplegic solution: a characterization in two species. *Scand. J. Thorac. Cardiovasc. Surg. Suppl.* 30:1–28.
40. Chen, J., W. Liu, …, X. Yu. 2005. Regional ventricular wall thickening reflects changes in cardiac fiber and sheet structure during contraction: quantification with diffusion tensor MRI. *Am. J. Physiol. Heart Circ. Physiol.* 289:H1898–H1907.
41. Munch, D. F., H. T. Comer, and J. M. Downey. 1980. Barium contracture: a model for systole. *Am. J. Physiol.* 239:H438–H442.
42. Hayashi, T., M. E. Martone, …, M. Hoshijima. 2009. Three-dimensional electron microscopy reveals new details of membrane systems for Ca^{2+} signaling in the heart. *J. Cell Sci.* 122:1005–1013.
43. Suzuki, S., T. Tsuchiya, …, H. Sugi. 1989. Electron microscopic studies on the stretch-induced disordering of the myofilament lattice in tetanized frog skeletal muscle fibers. *J. Electron Microsc. (Tokyo).* 38:60–63.
44. Wu, X., Y. Yang, …, M. J. Davis. 2008. Potentiation of large conductance, Ca^{2+}-activated K^+ (BK) channels by $\alpha5\beta1$ integrin activation in arteriolar smooth muscle. *J. Physiol.* 586:1699–1713.
45. Sun, Z., L. A. Martinez-Lemus, …, G. A. Meininger. 2005. Mechanical properties of the interaction between fibronectin and $\alpha5\beta1$-integrin on vascular smooth muscle cells studied using atomic force microscopy. *Am. J. Physiol. Heart Circ. Physiol.* 289:H2526–H2535.
46. Lehenkari, P. P., and M. A. Horton. 1999. Single integrin molecule adhesion forces in intact cells measured by atomic force microscopy. *Biochem. Biophys. Res. Commun.* 259:645–650.

47. Costandi, P. N., L. R. Frank, …, J. H. Omens. 2006. Role of diastolic properties in the transition to failure in a mouse model of the cardiac dilatation. *Am. J. Physiol. Heart Circ. Physiol.* 291: H2971–H2979.

48. Doll, S., and K. Schweizerhof. 2000. On the development of volumetric strain energy functions. *J. Appl. Mech.* 67:17–21.

49. Guccione, J. M., A. D. McCulloch, and L. K. Waldman. 1991. Passive material properties of intact ventricular myocardium determined from a cylindrical model. *J. Biomech. Eng.* 113:42–55.

50. Kerckhoffs, R. C., M. L. Neal, …, A. D. McCulloch. 2007. Coupling of a 3D finite element model of cardiac ventricular mechanics to lumped systems models of the systemic and pulmonic circulation. *Ann. Biomed. Eng.* 35:1–18.

51. Sonnenblick, E. H., and C. L. Skelton. 1974. Reconsideration of the ultrastructural basis of cardiac length-tension relations. *Circ. Res.* 35:517–526.

52. Craig, R., and J. L. Woodhead. 2006. Structure and function of myosin filaments. *Curr. Opin. Struct. Biol.* 16:204–212.

Novel Role for Vinculin in Ventricular Myocyte Mechanics and Dysfunction

Jared R. Tangney,[†△] Joyce S. Chuang,[†△] Matthew S. Janssen,[†] Adarsh Krishnamurthy,[†] Peter Liao,[‡§] Masahiko Hoshijima,[‡‡‡] Xin Wu,[¶] Gerald A. Meininger,[‖] Mariappan Muthuchamy,[¶] Alice Zemljic-Harpf,[‡§] Robert S. Ross,[‡§‡‡] Lawrence R. Frank,[††] Andrew D. McCulloch,[†‡‡‡] and Jeffrey H. Omens[†‡‡‡*]

[†]Department of Bioengineering, [‡]Department of Medicine, University of California-San Diego, La Jolla, California; [§]Veterans Administration Healthcare San Diego, San Diego, California; [¶]Department of Systems Biology and Translational Medicine, Texas A&M Health Science Center, College of Medicine, College Station, Texas; [‖]Dalton Cardiovascular Research Center and Department of Medical Pharmacology and Physiology, University of Missouri, Columbia, Missouri; and [††]Department of Radiology, [‡‡]Cardiac Biomedical Science and Engineering Center, University of California-San Diego, La Jolla, California

Submitted August 22, 2012, and accepted for publication February 7, 2013.

SUPPORTING MATERIAL

MAGNET RESONANCE IMAGING (MRI)

MRI was performed on a 7T horizontal-bore magnet (Varian, Palo Alto, CA, USA) with an Avance II console (Bruker, Germany). Imaging protocols were based on methods in Chuang *et al.* (1). An ECG-triggered FLASH sequence was used for cine imaging with the following parameters: TE = 2.3 ms, TR = 6 ms, flip angle = 15°, slice thickness = 1 mm, NEX = 4, FOV = 2.0 cm, in-plane resolution = $(156\ \mu m)^2$. For MRI tagging, a spatial modulation of magnetization (SPAMM) sequence was used (2) to produce tag lines with a distance of 0.9 mm and width of 0.31 mm. Five short axis images and three longitudinal images were acquired. Cine and SPAMM images were collected at all slice locations. The entire imaging protocol took approximately 1 hour for each mouse (n=5 for both WT and KO hearts).

PAPILLARY MUSCLE STUDIES

Passive and active stress vs. strain curves for the papillary muscles were similar in magnitude and shape as those seen in WT hearts in previous studies with the same experimental setup (Sheikh, 2008, JCI). Passive stress was 0.48±0.30 kPa (WT) and 0.54±0.25 kPa (KO) at a strain of 0.1, and 1.84±1.29 kPa (WT) and 2.30±0.91 kPa (KO) at a strain of 0.2. Active stress was a nearly linear function of strain for both groups, with values of 18.36±8.52 kPa (WT) and 16.14±9.70 kPa (KO) at a strain of 0.2. For both active and passive function, neither showed a statistical effect of animal type on stress or an interaction of animal type and strain by ANOVA.

HISTOLOGY

After MRI imaging the hearts were arrested with a hyperkalemic solution and fixed with 10% buffered formalin as described previously (3). Each heart was cut into three pieces for fiber and sheet angle measurement. Each tissue piece was embedded in optimal cutting temperature compound and cryo-sectioned to produce 10 μm slices. The first block was sectioned through the LV free wall parallel to the epicardial circumferential-longitudinal plane (1-2) for transmural fiber angles (α). A continuous fiber angle distribution through the wall from epicardium to endocardium was calculated by a linear least squares fit of the measured α. The remaining tissue pieces were sectioned parallel to the circumferential radial (1-3) plane or the longitudinal-radial (2-3) surface, for measurement sheet angles (β) as described previously (3).

SAMPLE PREPARATION FOR TRANSMISSION ELECTRON MICROSCOPY (TEM)

The first group of the hearts (n=3 each cVclKO and WT) was arrested at end-diastole by perfusion with a modified St. Thomas' Hospital cardioplegic solution no. 2 (4); for the second group (n=3 each cVclKO and WT), barium contracture against zero-load was utilized to simulate end-systole (5, 6) by first perfusing the heart with a modified low-calcium Tyrode solution (0.078 mM $CaCl_2$) for 5 min and then Tyrode solution with 0.078 mM $CaCl_2$ and 2.5 mM $BaCl_2$. Tissue samples were then prepared as described previously with minor modifications (7). Briefly, the hearts were perfusion fixed with 2% (wt/v) paraformaldehyde and 2.5 % glutaraldehyde. Two-hundred μm thick vibratome slices were incubated in 0.8% potassium ferrocyanide and 2% osmium tetroxide overnight before being stained with 1% uranyl acetate (UA), dehydrated in ethanol, and embedded in Durcupan ACM resin.

MYOFILAMENT IMAGE ANALYSIS

Samples were prepared for TEM using standard techniques. Groups of cVclKO and WT hearts were fixed either in diastole (arrested) or in systole (barium contracture). 150-200 nm thickness sections for TEM were stained with 1% UA and Sato lead. Sets of images were obtained on a FEI Titan electron microscope operated at 300 kV. The tilt angle of the stage was adjusted manually such that the tissue was oriented for proper sectioning relative to the local fiber direction as quantified previously in the mouse (3). In order to quantify myofibril interfilament lattice spacing, images were recorded at 37,000x or 47,000x magnification by a Gatan 4K x 4K Ultrascan 4000 CCD camera with myocytes oriented approximately normal to the plane of the image. Sarcomere length (SL) images were recorded at 3,800x or 5,000x magnification by the same camera in the plane of the cell long axis. All images were processed within ImageJ. A square region of interest (ROI, 4096 by 4096 pixels) was selected at the A bands with both thick and thin filaments visible, and transformed into the spatial frequency domain by fast Fourier transformation (FFT). The distance to the first- and second-order diffraction patterns of the lattice images were converted into median inter-thick filament spacing and lattice spacing (thick to thin filament spacing) respectively across the region, while the first-order diffraction pattern from long axis sarcomere images was utilized to determine a median sarcomere length(8). A minimum of 12 ROIs was used in each animal for lattice spacing, and 18 ROIs from each for sarcomere length.

FLUORESCENCE CONFOCAL MICROSCOPY

Overnight cultured cardiac myocytes were fixed with 2% paraformaldehyde for one hour followed by several glycine-PBS washes. Cells were permeabilized with ice-cold methanol for 3

min at 4°C followed by several rinses with PBS. Cells were then incubated with blocking solution containing 1% BSA, 2.5% normal goat serum and 0.1% Triton X-100 for one hr. After the blocking step, cells were incubated together with primary mouse anti-vinculin (1:100, Chemicon International, Inc) or mouse IgG as control (1:100, Santa Cruz, CA) for one hour. Samples were rinsed and incubated with secondary antibodies of goat-anti-mouse Oregon green 488 IgG and goat-anti-rat red Cy5 IgG (1:200, Molecular Probes, Invitrogen) for 1 hour in the dark, washed extensively, and treated with ProLong AntiFade (Molecular Probes, Invitrogen). Serial image sections through focus with step size of 0.1-0.3 μm thickness were collected using the Leica AOBS SP2 Confocal microscope (Leica Microsystems GmbH Wetzlar, Germany). Normalized ratio of mean integrated fluorescent density of vinculin vs control IgG were compared.

ADHESION FORCE AND CELL STIFFNESS WITH AFM

AFM force mode operation for force and stiffness measurements

AFM was performed in adult male mouse cardiomyocytes that were isolated from wild-type C57BL/6 and heterozygous global Vcl null mice (2-4 months) hearts using methods described previously (9). In a third group vinculin gene transfer was performed in heterozygous null myocytes (10). Transient transfection of myocytes was carried out in 35 mm tissue culture dishes using the lipofection technique. LipofectAMINE(20 μl, Invitrogen, Gran Island, NY) was mixed with 5 μg of total plasmid cDNA containing both vinculin and enhanced green fluorescent protein cDNA in 4 ml of 2% (v/v) Dulbecco's modified Eagle's medium (DMEM) without penicillin and streptomycin serum-free DMEM and placed on cells for overnight at 37°C in a humidified incubator containing 5% CO2. . The cDNA-containing medium was then aspirated and replaced with 2.5 % DMEM with 100 U/ml penicillin and 100 μg/ml streptomycin. Enhanced green fluorescent protein was used to identify successful transfected cells that were used in AFM protocols. Only transfected cells were used for AFM protocols, typically 2-3 days after transfection. The force contact mode of operation was used to measure of adhesion and cortical membrane stiffness (elastic modulus) from the retraction and approach curves, respectively (11, 12). The AFM experiments were performed using a Bioscope system (Model 3A, Digital Instruments, Santa Barbara, CA), which was mounted on an Axiovert 100 TV inverted microscope (Carl Zeiss, Germany). The AFM probes were silicon nitride microlevers with pyramidal tips with 20 nm radius and mean spring constant approximately 14.4 ± 0.6 pN/nm (Veeco). For each experiment, the position of the protein (e.g. fibronectin (FN)) labeled probe was controlled to repeatedly touch and retract (Z-axis) from the cell membrane surface. Force curves were recorded for these repeated cycles of probe approach and retraction at 0.5 Hz scan frequency and a Z-axis movement of 800 nm. With each group of experiments, 500 force curves were sampled from 10 randomly selected cells (obtained from 3 to 5 hearts; 50 curves/cell) for each treatment.

To measure cell cortical stiffness (i.e., elastic modulus or cell resistance to shape deformation, Fig. S3), approach force curves were used for analysis (gray solid trace in Fig. S3). When the FN-coated probe moves to approach the cell surface (point 1 to 2), force remains at zero level. The cantilever will bend, encounter a resistance and change the deflection signal after contact with the surface (gray solid 'approach' line, point 2 to 3). Point 2 represents a 'reflection point or contact point'. The approach force curves were fitted with the Hertz Model assuming a cone shape indenting a flat surface between point 2 to 3 using MATLAB software (Mathwork, Inc.)

and NForceR software (copyright, 2004) to calculate the cortical stiffness based on tip displacement and membrane indentation. The stiffer the cell, the less the indentation and the steeper the upslope of the force curve. As the probe retraction starts (black dash 'retraction' line), the resistance force will decrease (point 3 to 4). The snap-off that represents bond rupture (i.e. termed adhesion force) between FN and the cardiomyocyte is shown in retraction line (black dash trace, point 5). To measure adhesion force, retraction force curves were used for analysis (solid dash trace in Fig. S3). Single-rupture forces were determined using Hooke's Law: $F=kd$. Where d is the height of the step change in the retraction curve representing bond rupture (in Fig. S3 point '5') and k is the spring constant (12, 13). The peak value (mode), which likely denotes a FN-integrin single bond unbinding force, represents the most frequent or maximum likelihood value obtained over 500 retraction curves in each experiment (11, 12, 14). A comparison of the FN adhesion force indicated that there was no difference among the three different regions, 25% from either end of the myocyte and in the lengthwise center of the cell (data not shown. Also see ref. (12)). As seen in Figure S3, the example trace shows two adhesion events (bond rupture) that occurred when the FN coated-probe retracted. When all adhesions between the FN-coated probe and cardiomyocyte have been broken, the retraction curve again overlies the initial approach curve level (point 6) because net forces acting on the cantilever are zero (i.e. equivalent to force acting on the probe during the approach).

Labeling of AFM probes

AFM probes were labeled with the FN, or control proteins using a method we have previously described (11, 12) that was adopted from Lehenkari and Horton (11, 13). Polyethylene glycol (PEG, Sigma) was used to cross-link proteins onto silicon nitride probes at room temperature. The probe was first incubated with 10 mg/ml PEG for 5 min, washed with phosphate buffered saline (PBS), and then incubated with FN (1 mg/ml, Invitrogen Corporation, Grand Island, NY) for 1 min. The tip was again washed with PBS. The spring constants were assumed to be unchanged after the protein labeling because only very end of the cantilever was coated. As a nonspecific protein, bovine serum albumin (BSA)-coated AFM probes were used. BSA coated probes (n=10) exhibited a significantly lower probability of binding and unbinding forces compared to FN coated probes (data not shown).

General data analysis

For adhesion force and stiffness measurement, NForceR program, Matlab software (MathWorks, Natick, MA), Origin (OriginLab Corporation), and SAS were used. Adhesion force between FN and integrins on myocyte plotted as a function of the frequency (events) of occurrence. Single-rupture forces were determined using Hooke's Law, with force being proportional to the height of the step change in the retraction curve representing bond rupture. Differences between means for the effect of a given treatment were determined using ANOVA, or with an independent two-tail t test, as appropriate. Averaged values were expressed as mean ± S.E.M.

MYOFILAMENT LATTICE MECHANICS MODEL

Cross-Bridge Stiffness Analysis

The single spring stiffness K of the S2 domain in the cross-bridge model can be resolved into fiber K_f and transverse K_t component stiffnesses by using the force balance equations(14) to derive the change in the axial (fiber) and radial (transverse) force components (F_f and F_t) due to

an infinitesimal change in the fiber and transverse displacement components in the strongly bound and strained state of the cross-bridge.

The forces acting along the S2 segment can be resolved as $F\cos\theta$ and $F\sin\theta$ along the fiber and transverse directions.

$$\begin{aligned} F_t &= F\sin\theta \\ F_f &= F\cos\theta \\ \frac{dF_t}{d\theta} &= \frac{dF}{d\theta}\sin\theta + F\cos\theta \\ \frac{dF_f}{d\theta} &= \frac{dF}{d\theta}\cos\theta - F\sin\theta \end{aligned} \tag{1}$$

Similarly, the displacements along the S2 segment can also be resolved into transverse and fiber components.

$$\begin{aligned} r &= l\sin\theta \\ x &= l\cos\theta \\ \frac{dr}{d\theta} &= \frac{dl}{d\theta}\sin\theta + l\cos\theta \\ \frac{dx}{d\theta} &= \frac{dl}{d\theta}\cos\theta - l\sin\theta \end{aligned} \tag{2}$$

From the definition of spring stiffness, $F = K(l_{S2} - \widehat{l}_{S2})$, where $\widehat{l}_{S2}$ is the rest length of the spring and l_{S2} is the strained length. For the transverse stiffness, dx=0, giving $\frac{dl}{d\theta} = l\tan\theta$ and $\frac{dr}{d\theta} = \frac{l}{\cos\theta}$, and hence:

$$\begin{aligned} \frac{dF}{d\theta} &= \frac{dF}{dl}\frac{dl}{d\theta} = Kl\tan\theta \\ \frac{dF_t}{d\theta} &= \frac{K(l - l_0\cos^2\theta)}{\cos\theta} \\ \frac{dF_t}{dr} &= \frac{dF_t}{d\theta}\frac{d\theta}{dr} \\ &= K\left(1 - \frac{l_0}{l}\cos^2\theta\right) \end{aligned} \tag{3}$$

Similarly, for the fiber stiffness, dr=0, $\frac{dl}{d\theta} = \frac{-l}{\tan\theta}$ and $\frac{dx}{d\theta} = \frac{-l}{\sin\theta}$, resulting in:

$$\begin{aligned}\frac{dF}{d\theta} &= \frac{dF}{dl}\frac{dl}{d\theta} = \frac{-Kl}{\tan\theta} \\ \frac{dF_f}{d\theta} &= \frac{-K(l - l_0\sin^2\theta)}{\sin\theta} \\ \frac{dF_f}{dx} &= \frac{dF_f}{d\theta}\frac{d\theta}{dx} \\ &= K\left(1 - \frac{l_0}{l}\sin^2\theta\right)\end{aligned} \tag{4}$$

From these two equations, we get the ratio of transverse to fiber stiffness to be given in terms of the S2 segment angle and lengths by:

$$\frac{K_t}{K_f} = \frac{\left(l - l_0\cos^2\theta\right)}{\left(l - l_0\sin^2\theta\right)} \tag{5}$$

Lattice Analysis

From the above analysis, the cross-bridges can be represented by equivalent fiber and transverse stiffnesses K_f and K_t, respectively. Assuming that the lattice is stretched in the perpendicular planes such that it deforms infinitesimally by u in both the axial (fiber) direction and the radial (transverse) direction, the energy stored due to deformation of a single spring structure is $\frac{1}{2}Ku^2$ where K is the stiffness in either the fiber or the transverse direction. There are six cross-bridges in each repeating hexagonal unit of the sarcomere (marked in yellow in Figure S4), leading to a total energy of $6\times\frac{1}{2}Ku^2$. The undeformed area of the hexagonal unit is $\frac{3\sqrt{3}}{2}\Delta_0^2$, where Δ_0 is the underformed lattice spacing. This gives an energy density (or the total energy per unit volume) in the unit cell with an axial length of δ_0 to be $\frac{1}{2}\left(\frac{4\sqrt{3}}{3}\right)\frac{K_f}{\delta_0}\left(\frac{u}{\Delta_0}\right)^2$ in the fiber and $\frac{1}{2}\left(\frac{4\sqrt{3}}{3}\right)\frac{K_t}{\delta_0}\left(\frac{u}{\Delta_0}\right)^2$ in the transverse directions, respectively.

Consider an isolated hexagonal unit cell that is deformed due to stretching of the cross-bridges. The lattice spacing changes by an infinitesimal magnitude u in the radial direction. The initial width of the unit cell is $\sqrt{3}\Delta_0$, and after deformation this width becomes $\sqrt{3}(\Delta_0 + u)$ or $\sqrt{3}\Delta$. Using a coordinate system with x_2 aligned with the unit cell width, the deformation gradient in the x_2 direction is $\left(1 + \frac{u}{\Delta_0}\right)$. Similarly, the deformation gradient in the x_3 direction is $\left(1 + \frac{u}{\Delta_0}\right)$.

The 2D deformation gradient tensor (**F**) and 2D finite strain tensor (**E**) can be expressed as

$$\mathbf{F} = \begin{bmatrix} 1+\dfrac{u}{\Delta_0} & 0 \\ 0 & 1+\dfrac{u}{\Delta_0} \end{bmatrix}$$
$$\mathbf{E} = \frac{1}{2}(\mathbf{F}^T\mathbf{F} - 1) = \begin{bmatrix} \dfrac{u}{\Delta_0}\left(1+\dfrac{u}{2\Delta_0}\right) & 0 \\ 0 & \dfrac{u}{\Delta_0}\left(1+\dfrac{u}{2\Delta_0}\right) \end{bmatrix} \tag{6}$$

Similarly, in the transverse direction, the deformation gradient is given by $\left(1+\dfrac{u}{\delta_0}\right)$ and the strain $\mathbf{E_{11}}$ by $\dfrac{u}{\delta_0}\left(1+\dfrac{u}{2\delta_0}\right)$.

Assuming a linear strain energy relation, we can equate the strain energy in a unit cell to the energy from the deformation of the cross-bridges in the transverse direction as $W = \dfrac{1}{2}C_t(E_{22}^2 + E_{33}^2)$, assuming that the transverse material stiffness C_t is constant (transversely isotropic) in the plane perpendicular to the actin/myosin filaments. Substituting the strain values, we can equate the strain energy.

$$W = \frac{1}{2}2C_t\left(\frac{u}{\Delta_0}\right)^2\left(1+\frac{u}{\Delta_0}+\frac{1}{4}\left(\frac{u}{\Delta_0}\right)^2\right) = \frac{1}{2}\left(\frac{4\sqrt{3}}{3}\right)\frac{K_t}{\delta_0}\left(\frac{u}{\Delta_0}\right)^2$$
$$\Rightarrow C_t = \frac{2\sqrt{3}}{3\delta_0\left(1+\dfrac{u}{\Delta_0}+\dfrac{1}{4}\left(\dfrac{u}{\Delta_0}\right)^2\right)}K_t \tag{7}$$

This gives the relation to the transverse material stiffness as a function of the transverse cross-bridge stiffness K_t, the lattice spacing Δ_0, the unit-cell axial spacing δ_0, and the cross-bridge lengthening the in the plane, u. Since u is small, we can neglect the square term leading to a simpler relation, $C_t = \dfrac{2}{\sqrt{3}}\dfrac{1}{\delta_0}\dfrac{\Delta_0}{\Delta}K_t$ where Δ is the deformed lattice spacing.

In the axial fiber direction, $W = \dfrac{1}{2}C_f E_{11}^2$ and again equating the energy in the fiber direction, we obtain:

$$W = \frac{1}{2} C_f \left(\frac{u}{\delta_0} \right)^2 \left(1 + \frac{u}{\delta_0} + \frac{1}{4} \left(\frac{u}{\delta_0} \right)^2 \right) = \frac{1}{2} \left(\frac{4\sqrt{3}}{3} \right) \frac{K_f}{\delta_0} \left(\frac{u}{\Delta_0} \right)^2$$

$$\Rightarrow C_f = \frac{4\sqrt{3}}{3\delta_0 \left(1 + \frac{u}{\delta_0} + \frac{1}{4} \left(\frac{u}{\delta_0} \right)^2 \right)} \left(\frac{\delta_0}{\Delta_0} \right)^2 K_f \tag{8}$$

which, upon linearization, yields $C_f = \frac{4}{\sqrt{3}} \frac{1}{\delta} \left(\frac{\delta_0}{\Delta_0} \right)^2 K_f$ and the macroscopic lattice stiffness ratio can be computed to be $\frac{C_t}{C_f} = \frac{1}{2} \left(\frac{\Delta_0}{\delta_0} \right)^3 \frac{\delta}{\Delta} \frac{K_t}{K_f}$.

The stress in the axial direction can be computed as $\sigma_{ff} = C_f E_{11}$ and in the transverse direction to be $\sigma_{tt} = C_r E_{22}$. This reduces to

$$\begin{aligned} \sigma_{ff} &= \frac{4\sqrt{3}}{3\delta_0 \left(1 + \frac{u}{\delta_0} + \frac{1}{4} \left(\frac{u}{\delta_0} \right)^2 \right)} \left(\frac{\delta_0}{\Delta_0} \right)^2 K_f \frac{u}{\delta_0} \left(1 + \frac{u}{2\delta_0} \right) \\ &= \frac{4\sqrt{3} u \delta_0}{3 \left(\delta_0 + \frac{u}{2} \right)} \left(\frac{1}{\Delta_0} \right)^2 K_f \end{aligned} \tag{9}$$

Similarly in the transverse direction

$$\sigma_{tt} = \frac{2\sqrt{3} u}{3\delta_0 \left(\Delta_0 + \frac{u}{2} \right)} K_t \tag{10}$$

and the transverse to fiber macroscopic peak systolic stress ratio is:

$$\frac{\sigma_{tt}}{\sigma_{ff}} = \frac{\dfrac{2\sqrt{3}u}{3\delta_0\left(\Delta_0+\dfrac{u}{2}\right)}K_t}{\dfrac{4\sqrt{3}u\delta_0}{3\left(\delta_0+\dfrac{u}{2}\right)}\left(\dfrac{1}{\Delta_0}\right)^2 K_f} = \frac{1}{2}\left(\frac{\Delta_0}{\delta_0}\right)^2 \frac{\left(\delta_0+\dfrac{u}{2}\right)}{\left(\Delta_0+\dfrac{u}{2}\right)}\frac{K_t}{K_f} \approx \frac{1}{2}\left(\frac{\Delta}{\delta}\right)\frac{K_t}{K_f} \tag{11}$$

The axial length of the unit cell is equal to the distance between 3 pairs of myosin heads (δ); in the lattice we get the stress ratio to be

$$\frac{\sigma_{tt}}{\sigma_{ff}} \approx \frac{1}{2}\left(\frac{\Delta}{\delta}\right)\frac{K_t}{K_f} \tag{12}$$

VENTRICULAR MECHANICS MODEL

To investigate the effect of sarcomere ultrastructural alterations due to Vcl deficiency on systolic wall mechanics, a finite element model of a mouse LV was created using a thick truncated ellipsoid of revolution (15). The focal length of the prolate spheroid was 3.75 mm. At zero pressure, the cavity volume of the mesh was 30 μl. The myocardium was modeled as a slightly compressible, transversely isotropic material with respect to the fiber and transverse-fiber directions (16). Average transmural fiber angle distributions measured in this study were used in the model. The unloaded geometry was passively inflated to an end-diastolic pressure of 10 mmHg.

Systolic material properties were obtained by adding active fiber and transverse stresses as functions of SL and time computed using the microstructural model described above. Resting myocardial material properties were modeled for both genotypes using a transversely isotropic exponential strain energy function (17). Length- and time-dependent contractile activation during systole was modeled using a model with parameters that were the same for both genotypes as given in Table S1. The LV was simulated to contract against a three-element Windkessel model (18) with an initial aortic pressure of 80 mmHg. Left ventricular and aortic pressures were used to determine closure of the aortic valve and the end-systolic time point. Thus this 3D functional model of the LV incorporated structural changes at the sarcomere level and was able to compute regional systolic strains in both WT and cVclKO models that could be compared with the MRI-derived measurements.

SUPPORTING FIGURES

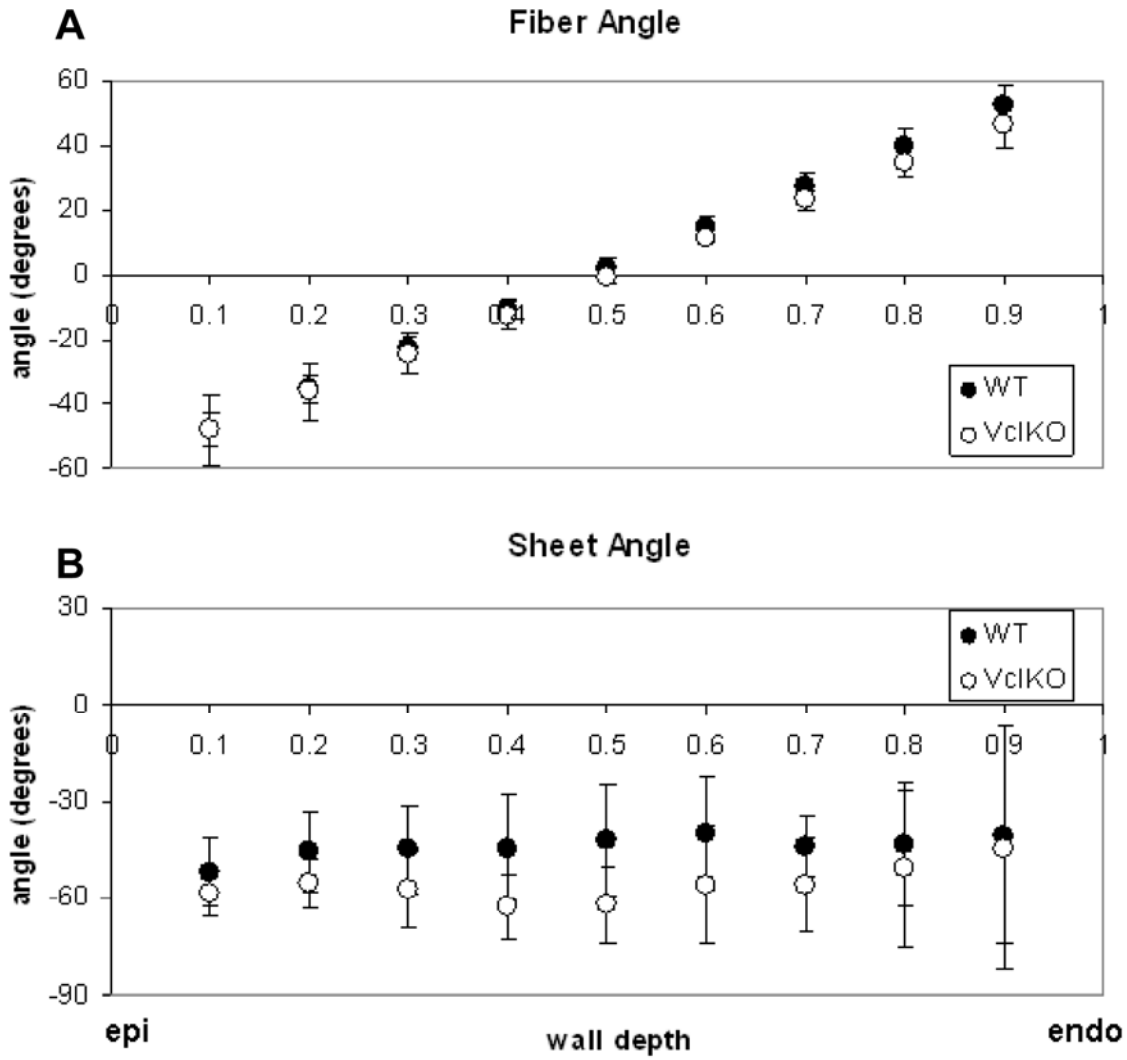

Figure S1: (A) Comparison of WT and VclKO transmural fiber angle distributions. (B) Comparison of WT and VclKO transmural sheet angle distributions.

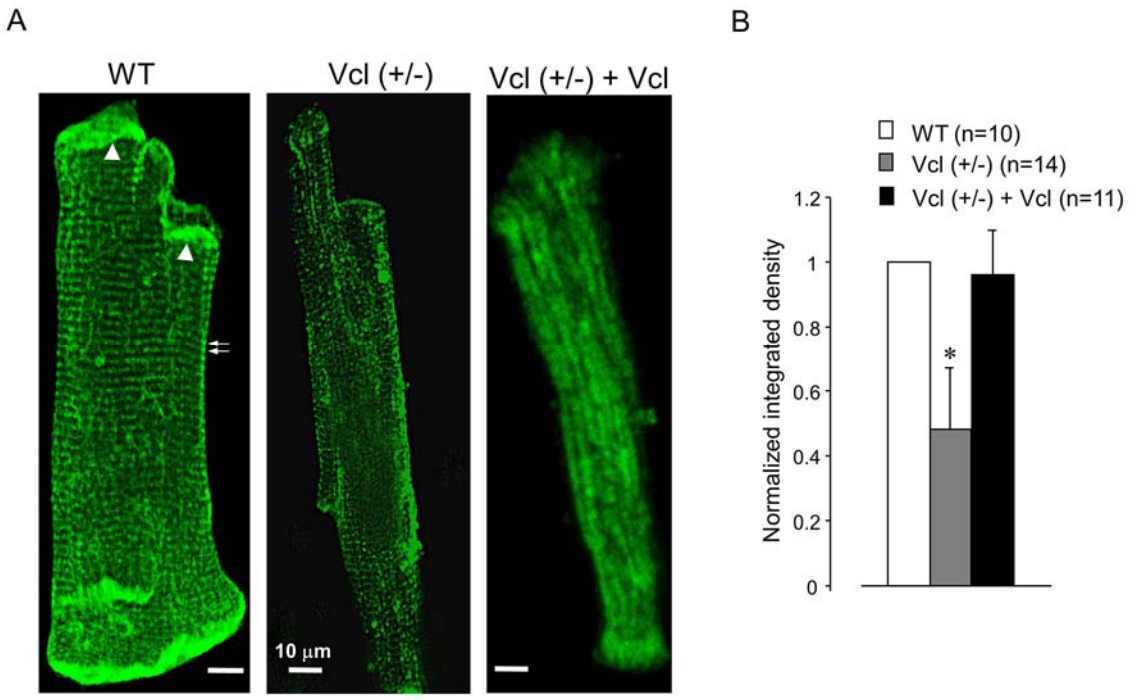

Figure S2: Immunofluorescence localization of cytoskeleton protein vinculin in cardiomyocytes from wild type adult mice (WT) and heterozygous null ((Vcl(+/-)), as well as GFP stained vinculin rescued [(Vcl(+/-) + Vcl] groups. (A) Isolated cardiac myocytes labeled green for vinculin with FITC-conjugated secondary antibody in WT and Vcl(+/-), or transfected cells expressing enhanced green fluorescent protein cDNA in [Vcl(+/-) + Vcl]. Vinculin staining is visualized at costameres (arrows, in cell edges) and intercalated disc (arrowheads). (B) Normalized mean integrated densities, i.e. normalized to control IgG staining or to non-transfected in each group before comparing among groups, were shown in cell body *$p<0.05$ vs. WT. The scale bar represents 10μm.

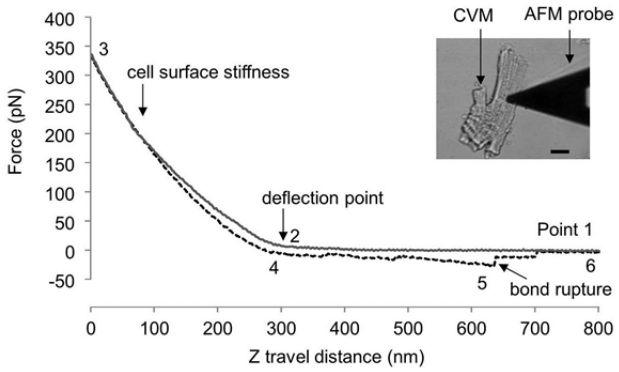

Figure S3: An example of a raw force curve generated using FN-coated AFM probe on cultured cardiomyocytes. FN-coated probes (1 mg/ml) were controlled to repeatedly (800 nm/s z-axis movement at 0.5 Hz frequency) approach (gray solid trace) and retract (black dash trace). The points 1 - 6 represent stages of approach and retraction (explained in detail in the supplemental section on AFM). Inserted image shows the AFM probe approaching the myocyte. Note the AFM cantilever is in sharp focus. CVM = cardiomyocyte.

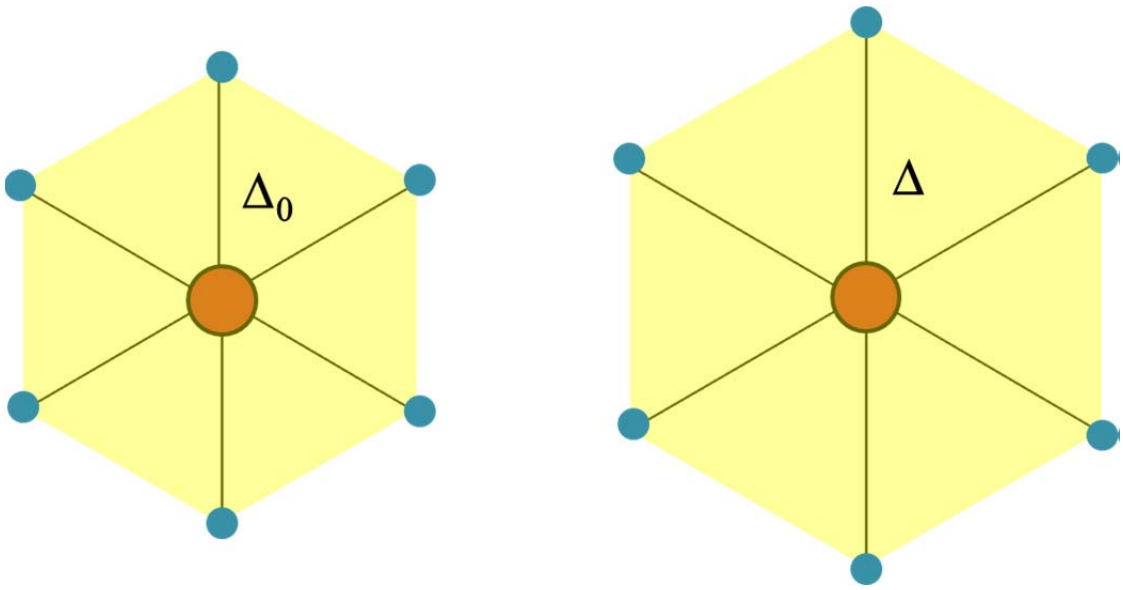

Figure S4: Isolated unit cell marked in yellow showing the actin and myosin filament cross-sections. The lattice spacing at rest is Δ_0. In the activated state, the lattice spacing is Δ.

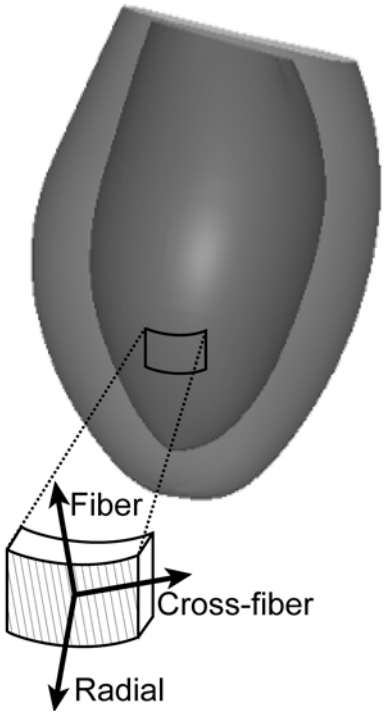

Figure S5: Fiber, cross-fiber, and radial coordinates used for strain analysis. Rotated from cardiac coordinates about the radial axis through the fiber angles. Fiber axis runs parallel to fibers, cross-fiber axis is in the same plane but perpendicular to fiber axis, and radial axis is orthogonal to the fiber-cross-fiber plane.

SUPPORTING TABLE

Parameter	Description	WT Value	cVclKO Value	Units	Source
k_spr	S2 spring constant	2	2	pN/nm	[19]
$\hat{l}_{S2}$	Unloaded S2 spring length	15	15	nm	*
l_{S2}	S2 resting length	18	18	nm	**
l_{S1}	S1 Length (projected)	11.3	11.3	nm	[14]
α	Axial angle of Attachment	45	45	deg	[14],[22]
Rm	radius of myosin	5.5	5.5	nm	[23]
Ra	radius of actin	3	3	nm	[23]
δ	Axial distance of 3 myosin head pairs	43.5	43.5	nm	[24]
V_s	Volume constant	1620	2030	$nm^{2*}\mu m$	EM Meas.
SL_unloaded	Relaxed unloaded sarcomere length	1.88	1.74	um	EM Meas.
SL_sys	Contracted unloaded sarcomere length	1.5	1.43	um	EM Meas.
S_f	EM shrinkage factor	1.2	1.2	n/a	[25]
Finite Element Model Parameters					
C	Stress scaling coefficient	0.88	0.88	n/a	[26]
bf	Fiber strain coefficient	18.5	18.5	n/a	[26]
bt	Transverse strain coefficient	3.58	3.58	n/a	[26]
bfs	Fiber-transverse-shear coefficient	1.63	1.63	n/a	[26]
bulk_mod	Bulk modulus	250	250	kPa	[18]
bcl	Basic cycle length	600	600	ms	[18]
bten	Governs shape of peak isometric tension-SL relation	1.8	1.8	1/μm	[18]
c0max	Maximum intracellular calcium concentration	4.35	4.35	μM	[26]
c0	Peak intracellular calcium concentration	4.35	4.35	μM	[26]
tmax	Isometric tension under maximal activation	137.5	137.5	kPa	[26]
dur	Scales duration of contraction	0.25	0.25	n/a	[18]
rmc	Slope of twitch contraction	52.49	52.49	ms/μm	[18]
bc	Offset of twitch contraction	55.26	55.26	ms	[18]
rmr	Slope of twitch relaxation	131.2	131.2	ms/μm	[18]
br	Offset of twitch relaxation	-94.34	-94.34	ms	[18]
c_act	Arbitrary stress scaling factor	77	77	n/a	

** Parameter value derived from projections of a 3-dimensional model using values from Williams et. al. (19), to the 2-dimensional model that is used here.

* Parameter value derived from new 2-dimensional model lengths.

Table S1. Model parameters used in the micromechanical and finite element models.

SUPPORTING REFERENCES (18-26)

1. Chuang, J. S., A. Zemljic-Harpf, R. S. Ross, L. R. Frank, A. D. McCulloch, and J. H. Omens. 2010. Determination of three-dimensional ventricular strain distributions in gene-targeted mice using tagged MRI. Magn Reson Med 64:1281-1288.
2. Axel, L., and L. Dougherty. 1989. MR imaging of motion with spatial modulation of magnetization. Radiology 171:841-845.
3. Omens, J. H., T. P. Usyk, Z. Li, and A. D. McCulloch. 2002. Muscle LIM protein deficiency leads to alterations in passive ventricular mechanics. Am J Physiol Heart Circ Physiol 282:H680-H687.
4. Jynge, P., D. J. Hearse, D. Feuvray, W. Mahalu, S. Cankovic-Darracott, K. O'Brien, and M. V. Braimbridge. 1981. The St. Thomas' hospital cardioplegic solution: a characterization in two species. Scand J Thorac Cardiovasc Surg Suppl 30:1-28.
5. Chen, J., W. Liu, H. Zhang, L. Lacy, X. Yang, S. Song, S. A. Wickline, and X. Yu. 2005. Regional ventricular wall thickening reflects changes in cardiac fiber and sheet structure during contraction: quantification with diffusion tensor MRI. Am J Physiol Heart Circ Physiol 289:H1898-H1907.
6. Munch, D. F., H. T. Comer, and J. M. Downey. 1980. Barium contracture: a model for systole. Am J Physiol Heart Circ Physiol 239:H438-H442.
7. Hayashi, T., M. E. Martone, Z. Yu, A. Thor, M. Doi, M. J. Holst, M. H. Ellisman, and M. Hoshijima. 2009. Three-dimensional electron microscopy reveals new details of membrane systems for Ca2+ signaling in the heart. J Cell Sci 122:1005-1013.
8. Suzuki, S., T. Tsuchiya, Y. Oshimi, T. Takei, and H. Sugi. 1989. Electron microscopic studies on the stretch-induced disordering of the myofilament lattice in tetanized frog skeletal muscle fibers. J Electron Microsc (Tokyo) 38:60-63.
9. Wu, X., S. Chakraborty, C. L. Heaps, M. J. Davis, G. A. Meininger, and M. Muthuchamy. 2011. Fibronectin increases the force production of mouse papillary muscles via alpha5beta1 integrin. J Mol Cell Cardiol 50:203-213.
10. Wu, X., Y. Yang, P. Gui, Y. Sohma, G. A. Meininger, G. E. Davis, A. P. Braun, and M. J. Davis. 2008. Potentiation of large conductance, Ca2+-activated K+ (BK) channels by alpha5beta1 integrin activation in arteriolar smooth muscle. The Journal of physiology 586:1699-1713.
11. Sun, Z., L. A. Martinez-Lemus, A. Trache, J. P. Trzeciakowski, G. E. Davis, U. Pohl, and G. A. Meininger. 2005. Mechanical properties of the interaction between fibronectin and alpha5beta1-integrin on vascular smooth muscle cells studied using atomic force microscopy. Am J Physiol Heart Circ Physiol 289:H2526-2535.
12. Wu, X., Z. Sun, A. Foskett, J. P. Trzeciakowski, G. A. Meininger, and M. Muthuchamy. 2010. Cardiomyocyte contractile status is associated with differences in fibronectin and integrin interactions. Am J Physiol Heart Circ Physiol 298:H2071-2081.
13. Lehenkari, P. P., and M. A. Horton. 1999. Single integrin molecule adhesion forces in intact cells measured by atomic force microscopy. Biochem Biophys Res Commun 259:645-650.
14. Schoenberg, M. 1980. Geometrical factors influencing muscle force development: I. The effect of filament spacing upon axial forces. Biophys J 30:51-68.
15. Costandi, P. N., L. R. Frank, A. D. McCulloch, and J. H. Omens. 2006. Role of diastolic properties in the transition to failure in a mouse model of the cardiac dialation. Am J Physiol Heart Circ Physiol 291:H2971-H2979.

16. Doll, S., and K. Schweizerhof. 2000. On the development of volumetric strain energy functions. J Appl Mech 67:17-21.
17. Guccione, J. M., A. D. McCulloch, and L. K. Waldman. 1991. Passive material properties of intact ventricular myocardium determined from a cylindrical model. J Biomech Eng 113:42-55.
18. Kerckhoffs, R. C., M. L. Neal, Q. Gu, J. B. Bassingthwaighte, J. H. Omens, and A. D. McCulloch. 2007. Coupling of a 3D finite element model of cardiac ventricular mechanics to lumped systems models of the systemic and pulmonic circulation. Ann Biomed Eng 35:1-18.
19. Williams, C. D., M. Regnier, and T. L. Daniel. 2010. Axial and radial forces of cross-bridges depend on lattice spacing. PLoS Comput Biol 6:e1001018.
20. Matsubara, I., and B. M. Millman. 1974. X-ray diffraction patterns from mammalian heart muscle. J Mol Biol 82:527-536.
21. Rayment, I., H. M. Holden, M. Whittaker, C. B. Yohn, M. Lorenz, K. C. Holmes, and R. A. Milligan. 1993. Structure of the actin-myosin complex and its implications for muscle contraction. Science 261:58-65.
22. Julian, F. J., R. L. Moss, and M. R. Sollins. 1978. The mechanism for vertebrate striated muscle contraction. Circ Res 42:2-14.
23. Sonnenblick, E. H., and C. L. Skelton. 1974. Reconsideration of the ultrastructural basis of cardiac length-tension relations. Circ Res 35:517-526.
24. Craig, R., and J. L. Woodhead. 2006. Structure and function of myosin filaments. Curr Opin Struct Biol 16:204-212.
25. Millman, B. M. 1998. The filament lattice of striated muscle. Physiol Rev 78:359-391.
26. Guccione, J. M., L. K. Waldman, and A. D. McCulloch. 1993. Mechanics of active contraction in cardiac muscle. J Biomech Eng 115:72-90.